Collider signatures of fermionic scotogenic dark matter

Víctor Martín Lozano,[1,2,*] G. Sanchez Garcia,[1,2,†] and J. W. F. Valle[1,‡]

[1]*AHEP Group, Institut de Física Corpuscular—CSIC/Universitat de València, Parc Cientific de Paterna, C/Catedratico José Beltrán, 2 E-46980 Paterna (València), Spain*

[2]*Departament de Física Teòrica, Universitat de València, 46100 Burjassot, Spain*

(Received 24 February 2025; accepted 26 July 2025; published 4 September 2025)

Weakly interacting massive particles (WIMPs) constitute a paradigm in the search for particle dark matter. In contrast to supersymmetry (SUSY), we explore the possibility that WIMP dark matter acts as mediator of neutrino mass generation. We examine in detail the phenomenology of fermionic dark matter in the revamped (or singlet-triplet) scotogenic model and study its collider implications. Unlike SUSY WIMP dark matter, collider searches for the lightest scotogenic particle at LHC/LHC-HL are strongly complementary to charged lepton flavor violation probes and dark matter studies.

DOI: 10.1103/73xh-7hhz

I. INTRODUCTION

The experimental discovery of neutrino oscillations [1,2] provides unambiguous proof that neutrinos are massive, indicating the need for new physics, beyond the Standard Model (SM). On the other hand, there is clear evidence in favor of the existence of dark matter in our Universe [3], whose origin is still unknown, opening a window to new physics searches. The ultimate origin of neutrino masses and the explanation of cosmological dark matter constitute two fundamental challenges for our current understanding of basic particle physics and cosmology. If neutrinos acquire mass in the same way as other SM fermions via the Higgs mechanism, then one requires very tiny Yukawa couplings so as to match the observed tiny neutrino masses. Alternatively, small neutrino masses may result from the exchange of very heavy mediators, such as various realizations of the seesaw mechanism. Whichever way, however, these scenarios are difficult to probe at particle colliders.

An interesting idea is that neutrino masses result from the radiative exchange of "dark states" that may lie in the TeV scale [4,5]. The scotogenic approach now constitutes one of the current paradigms in neutrino mass generation, with a very extensive literature. See, for example, Refs. [6–23]. Within such scotogenic scenarios, dark matter and neutrino masses are explained at the same time. The basic idea is to introduce "dark" fields, odd under a postulated $\mathbb{Z}_2$ symmetry that makes dark matter stable, while accounting for the radiative origin neutrino mass. This scenario is phenomenologically attractive since it allows for small neutrino masses with relatively sizable Yukawa coupling strengths. It leads naturally to a weakly interacting massive particle (WIMP) dark matter scenario for which there are, in general, three approaches to explore, as depicted in the diagram of Fig. 1.

Here we consider the phenomenology of the simplest generalization of the scotogenic model. Such "revamped" model, also called the singlet-triplet scotogenic model, was first introduced in Ref. [24] and explored in many subsequent works. This generalized setup requires the presence of a triplet scalar, along with a triplet fermion, absent in the original model [4,5]. Altogether, this revamped scheme has a doublet and a triplet scalar, along with a singlet and a triplet fermion, and is often called the singlet-triplet scotogenic model. The two dark fermions can be naturally associated with the two observed oscillation lengths, determined by the solar

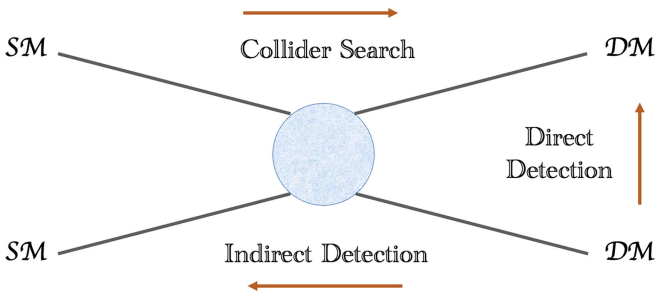


FIG. 1. Dark matter (DM) searches diagram.

*Contact author: victor.lozano@ific.uv.es
†Contact author: gsanchez@ific.uv.es
‡Contact author: valle@ific.uv.es

Published by the American Physical Society under the terms of the Creative Commons Attribution 4.0 International license. Further distribution of this work must maintain attribution to the author(s) and the published article's title, journal citation, and DOI. Funded by SCOAP³.

and atmospheric mass splittings [25], leaving one neutrino as massless, a characteristic feature of the "missing partner" seesaw mechanism [26] realized here in a radiative manner. This has the important consequence that neutrinoless double β decay may be detectable in the next round of experiments [27–29].

Scotogenic models may harbor either scalar or fermionic dark matter. Scalar dark matter in the revamped scotogenic model has been extensively explored in Ref. [30], so here we focus on the detection prospects of fermionic scotogenic dark matter. Direct detection through nuclear recoil has been extensively studied in Ref. [31], while the prospects for indirect detection will be discussed elsewhere. Given the improved sensitivities already reached, here we focus on collider searches, where the interaction of high-energy SM particles result in the production of scotogenic states, which eventually decay into the fermionic dark matter plus SM particles, leaving signals at collider detectors. Our present goal is therefore to address the collider prospects of the revamped scotogenic model, extending the work of Ref. [31].

The remainder of the paper is structured as follows: in Sec. II, we provide the basics of the revamped scotogenic model, discussing its scalar and fermion sectors, along with the neutrino mass generation. In Sec. III, we discuss constraints on the parameter space that follow from theoretical arguments, as well as from neutrino oscillation data, charged lepton flavor violation (cLFV) and electroweak precision tests. In Sec. IV, we discuss signatures at colliders, current limits, and future sensitivities, giving our conclusions in Sec. V.

TABLE I. Particle content of the revamped scotogenic model and the quantum number assignments.

	Standard model			New scalars		New fermions	
Gauge group	L	e	ϕ	η	Ω	F	Σ
$SU(3)_C$	1	1	1	1	1	1	1
$SU(2)_L$	2	1	2	2	3	1	3
$U(1)_Y$	$-1/2$	1	$1/2$	$1/2$	0	0	0
Z_2	$+$	$+$	$+$	$-$	$+$	$-$	$-$
Multiplicities	3	3	1	1	1	1	1

II. THE REVAMPED SCOTOGENIC MODEL

Here we consider the singlet-triplet scotogenic model as a revamped version of the original scotogenic model [4,5]. It extends the SM of particle physics by introducing additional scalar and fermionic degrees of freedom. The theory includes a new singlet fermion F and a triplet Σ under $SU(2)_L$, with no hypercharge and no color. The extra scalars, also singlets under $SU(3)_c$, are a doublet η and a triplet Ω under $SU(2)_L$, with hypercharges $1/2$ and 0, respectively. Moreover, one imposes a $\mathbb{Z}_2$ discrete symmetry, under which F, Σ, and η have an odd charge, while the rest of the particles are even. This ensures the stability of the lightest dark particle, assumed here to be a fermion, making it a potential dark matter candidate [31]. We refer to it as the lightest scotogenic particle (LSP). A summary of the particle content of the theory, with the corresponding quantum number assignments, is given in Table I.

The Lagrangian describing the lepton interactions, and hence, responsible for the neutrino mass generation, is given by

$$\mathcal{L} \subset -Y^{\alpha\beta} L_\alpha \phi e_\beta - Y_F^\alpha (\bar{L}_\alpha \tilde{\eta}) F - Y_\Sigma^\alpha \bar{L}_\alpha^c \Sigma^\dagger \tilde{\eta} - Y_\Omega \mathrm{Tr}\,[\bar{\Sigma}\Omega] F - \frac{1}{2} M_\Sigma \mathrm{Tr}(\bar{\Sigma}^c \Sigma) - \frac{M_F}{2} \bar{F}^c F + \mathrm{H.c.}, \tag{1}$$

where M_F and M_Σ are mass parameters, L_α are the SM lepton doublets, and we have defined $\tilde{\eta} = i\sigma_2 \eta^*$. Here α, β are flavor indices (e, μ, τ), and $Y^{\alpha\beta}$, Y_F^α, Y_Σ^α, and Y_Ω are the Yukawa couplings, with $Y^{\alpha\beta}$ denoting the usual SM lepton Yukawas, assumed to be diagonal in flavor.

A. Scalar sector

The most general scalar potential invariant under $SU(2)_L \times U(1)_Y \times \mathbb{Z}_2$ can be written as

$$\begin{aligned} V = & -m_\phi^2 \phi^\dagger \phi + m_\eta^2 \eta^\dagger \eta - \frac{m_\Omega^2}{2} \mathrm{Tr}(\Omega^\dagger \Omega) + \frac{\lambda_1}{2} (\phi^\dagger \phi)^2 + \frac{\lambda_2}{2} (\eta^\dagger \eta)^2 + \frac{\lambda_3}{2} (\phi^\dagger \phi)(\eta^\dagger \eta) \\ & + \lambda_4 (\phi^\dagger \eta)(\eta^\dagger \phi) + \frac{\lambda_5}{2} [(\phi^\dagger \eta)^2 + (\eta^\dagger \phi)^2] + \mu_1 \phi^\dagger \Omega \phi + \mu_2 \eta^\dagger \Omega \eta \\ & + \frac{\lambda_1^\Omega}{2} (\phi^\dagger \phi) \mathrm{Tr}(\Omega^\dagger \Omega) + \frac{\lambda_2^\Omega}{4} [\mathrm{Tr}(\Omega^\dagger \Omega)]^2 + \frac{\lambda_\eta^\Omega}{2} (\eta^\dagger \eta) \mathrm{Tr}(\Omega^\dagger \Omega), \end{aligned} \tag{2}$$

where one sees the terms involving the new scalar fields, η and Ω. Here $\lambda_{1,2,3,4,5}$, and $\lambda_{1,2,\eta}^\Omega$ are dimensionless, while μ_1, μ_2, m_ϕ, m_Ω, and m_η have mass dimensions.

To ensure that the potential in Eq. (2) is bounded from below, the λ parameters must fulfill several conditions given in [30–33] and that we list below,

$$\lambda_1 \geq 0, \qquad \lambda_2 \geq 0, \qquad \lambda_2^{\Omega} \geq 0, \qquad \lambda_3 + \sqrt{\lambda_1 \lambda_2} \geq 0, \qquad \lambda_3 + \lambda_4 - |\lambda_5| + \sqrt{\lambda_1 \lambda_2} \geq 0,$$
$$\lambda_1^{\Omega} + \sqrt{2\lambda_1 \lambda_2^{\Omega}} \geq 0, \qquad \lambda_\eta^{\Omega} + \sqrt{2\lambda_2 \lambda_2^{\Omega}},$$
$$\sqrt{2\lambda_1 \lambda_2 \lambda_2^{\Omega}} + \lambda_3 \sqrt{2\lambda_2^{\Omega}} + \lambda_1^{\Omega} \sqrt{\lambda_2} + \lambda_\eta^{\Omega} \sqrt{\lambda_1} + \sqrt{(\lambda_3 + \sqrt{\lambda_1 \lambda_2}) \left(\lambda_1^{\Omega} + 2\sqrt{\lambda_1 \lambda_2^{\Omega}}\right) \left(\lambda_\eta^{\Omega} + \sqrt{\lambda_2 \lambda_2^{\Omega}}\right)} \geq 0. \tag{3}$$

In addition, we require all quartic couplings of Eq. (2) to have values $\leq \sqrt{4\pi}$ so that a perturbative expansion of the potential around its minimum is justified.[1]

Assuming m_ϕ^2, m_η^2, and m_Ω^2 to be positive, one has that the spontaneous electroweak symmetry breaking (EWSB) is driven only by the neutral components of ϕ (and Ω). This way only the fields ϕ and Ω will acquire nonvanishing vacuum expectation values (VEVs), and we denote

$$\langle \phi^0 \rangle = v_\phi, \qquad \langle \Omega^0 \rangle = v_\Omega, \qquad \langle \eta^0 \rangle = 0, \tag{4}$$

where the nonzero VEVs must satisfy the condition $v_\phi^2 + v_\Omega^2 = v^2 \sim (246)^2$ GeV^2 to agree with experimental observations. The scalar doublet η does not acquire a VEV, so that the $\mathbb{Z}_2$ symmetry is preserved after EWSB takes place.

After EWSB, the scalar fields can be written as

$$\eta = \begin{pmatrix} \eta^+ \\ (\eta_R + \eta_I)/\sqrt{2} \end{pmatrix}, \quad \phi = \begin{pmatrix} \varphi^+ \\ (h^0 + v_\phi + i\varphi^0)/\sqrt{2} \end{pmatrix}, \qquad \Omega = \begin{pmatrix} (\Omega^0 + v_\Omega)/\sqrt{2} & \Omega^+ \\ \Omega^- & -(\Omega^0 + v_\Omega)/\sqrt{2} \end{pmatrix}. \tag{5}$$

Then, minimization of the potential leads to the tadpole equations

$$\frac{\partial V}{\partial \phi} = \frac{1}{2} v_\phi (-2m_\phi^2 + \lambda_1 v_\phi^2 + v_\Omega (\lambda_1^{\Omega} v_\Omega - \sqrt{2}\mu_1)) = 0, \tag{6}$$

$$\frac{\partial V}{\partial \Omega} = \frac{1}{4} (-4m_\Omega v_\Omega + 4\lambda_2^{\Omega} v_\Omega^3 + v_\phi^2 (2\lambda_1^{\Omega} v_\Omega - \sqrt{2}\mu_1)) = 0, \tag{7}$$

$$\frac{\partial V}{\partial \eta_R} = 0. \tag{8}$$

From the Lagrangian in Eq. (1), we can write the CP-even neutral scalar mass-squared matrix,

$$\mathcal{M}_h^2 = \begin{pmatrix} -m_\phi^2 + \frac{3}{2}\lambda_1 v_\phi^2 + \frac{v_\Omega}{2}(-\sqrt{2}\mu_1 + \lambda_1^{\Omega} v_\Omega) & v_\phi \left(\lambda_1^{\Omega} v_\Omega - \frac{\mu_1}{\sqrt{2}}\right) \\ v_\phi \left(\lambda_1^{\Omega} v_\Omega - \frac{\mu_1}{\sqrt{2}}\right) & 3\lambda_2^{\Omega} v_\Omega^2 + \frac{1}{2}\lambda_1^{\Omega} v_\phi^2 - m_\Omega^2 \end{pmatrix}, \tag{9}$$

which extends that of the SM. After applying the tadpole conditions evaluated at the VEVs, we can write

$$\mathcal{M}_h^2 = \begin{pmatrix} \lambda_1 v_\phi^2 & \frac{1}{\sqrt{2}} v_\phi (\lambda_1^{\Omega} v_\Omega - \mu_1) \\ \frac{1}{\sqrt{2}} v_\phi (\lambda_1^{\Omega} v_\Omega - \mu_1) & 2\lambda_2^{\Omega} v_\Omega^2 + \frac{1}{2\sqrt{2}} \mu_1 \frac{v_\phi^2}{v_\Omega} \end{pmatrix}. \tag{10}$$

Diagonalization of this matrix leads to two neutral states. The lightest one, denoted as h, is identified as the SM-like Higgs boson with mass $m_h = 125$ GeV. The heaviest of these states is denoted as H. Likewise, from the Lagrangian in Eq. (1), we can write the charged Higgs boson squared-mass matrix of our model as

$$\mathcal{M}_{H^\pm}^2 = \begin{pmatrix} -m_\phi^2 + \frac{\lambda_1 v_\phi^2}{2} + \frac{v_\Omega}{2}(\lambda_1^{\Omega} v_\Omega + \sqrt{2}\mu_1) & \frac{\mu_1 v_\phi}{\sqrt{2}} \\ \frac{\mu_1 v_\phi}{\sqrt{2}} & -m_\Omega^2 + \frac{\lambda_1^{\Omega} v_\phi^2}{2} + \lambda_2^{\Omega} v_\Omega^2 \end{pmatrix}, \tag{11}$$

[1]Further constraints are imposed to the potential, so that the renormalization group evolution does not break the $\mathbb{Z}_2$ symmetry at higher energies [32].

which can be simplified by using the tadpole equations, giving as a result

$$\mathcal{M}^2_{H^\pm} = \sqrt{2}\mu_1 \begin{pmatrix} v_\Omega & \frac{v_\phi}{2} \\ \frac{v_\phi}{2} & \frac{1}{4}\frac{v_\phi^2}{v_\Omega} \end{pmatrix}, \tag{12}$$

By diagonalizing this matrix, we get the mass of the charged Higgs boson (absent in the SM)

$$m_{H^\pm} = \mu_1 \frac{(v_\phi^2 + 2v_\Omega^2)}{2v_\Omega}. \tag{13}$$

Since the early days of the triplet seesaw mechanism it has been known that the Standard Model gauge boson mass relation is, in general, modified due to the presence of the Higgs triplet scalar [26]. In our case, since the triplet Higgs Ω is real (no hypercharge), the Z boson acquires its longitudinal component only from the Higgs doublet ϕ. In contrast, however, the charged Goldstone boson is a combination of ϕ^+ and Ω^+, so that the W boson mass gets contributions from both Higgs scalars,

$$m_Z^2 = \frac{1}{4}(g^2 + g'^2)v_\phi^2, \tag{14}$$

$$m_W^2 = \frac{1}{4}g^2(v_\phi^2 + 4v_\Omega^2). \tag{15}$$

The modified gauge boson mass relation results in an upper limit for the triplet scalar VEV, $v_\Omega \leq 5$ GeV [34,35]. The small value of v_Ω suggests a small mixing between the singlet and triplet dark fermions, see Eq. (19) below.

Concerning the dark $SU(2)_L$ scalar doublet η, the charged state does not mix, so that

$$m^2_{\eta^+} = m_\eta^2 + \frac{1}{2}\lambda_3 v_\phi^2 + \frac{1}{\sqrt{2}}\mu_2 v_\Omega + \frac{1}{2}\lambda_\eta^\Omega v_\Omega^2. \tag{16}$$

On the other hand, for the real and imaginary components of the neutral scalars one has

$$m^2_{\eta_R} = m_\eta^2 + \frac{1}{2}(\lambda_3 + \lambda_4 + \lambda_5)v_\phi^2 + \frac{1}{2}\lambda_\eta^\Omega v_\Omega^2 - \frac{1}{\sqrt{2}}\mu_2 v_\Omega \tag{17}$$

and

$$m^2_{\eta_I} = m_\eta^2 + \frac{1}{2}(\lambda_3 + \lambda_4 - \lambda_5)v_\phi^2 + \frac{1}{2}\lambda_\eta^\Omega v_\Omega^2 - \frac{1}{\sqrt{2}}\mu_2 v_\Omega. \tag{18}$$

The mass difference between the real and imaginary parts is determined by the parameter λ_5, $\Delta m_\eta = m_{\eta_R} - m_{\eta_I} = \lambda_5 v_\Omega$. In the limit $\lambda_5 \to 0$, the theory has a higher symmetry corresponding to lepton number and, as we will see, neutrinos become massless. Small neutrino masses are hence natural *à la* 't Hooft [36], protected by lepton number conservation. Hence, λ_5 must be small in order to explain the small neutrino masses, implying that the dark neutral scalars are nearly degenerate in mass.

B. Fermion sector

Given that Ω acquires a nonzero v_Ω, after EWSB takes place, the fermion singlet F mixes with the neutral component of the fermion triplet Σ through the Lagrangian term $Y_\Omega \mathrm{Tr}\,[\bar{\Sigma}\Omega]F$. The corresponding mass matrix reads

$$m_{\chi^0} = \begin{pmatrix} M_\Sigma & v_\Omega Y_\Omega \\ v_\Omega Y_\Omega & M_F \end{pmatrix}. \tag{19}$$

Assuming CP conservation in the fermionic scotogenic sector, we can diagonalize this matrix to the physical states denoted as $\chi^0_{1,2}$, with masses

$$m_{\chi^0_{1,2}} = \frac{1}{2}\left(M_\Sigma + M_F \mp \sqrt{(M_\Sigma - M_F)^2 + 4(2Y_\Omega v_\Omega)^2}\right). \tag{20}$$

To get these states, we have performed a orthogonal transformation with angle $\tan 2\theta = 2Y_\Omega v_\Omega/(M_\Sigma - M_F)$. On the other hand, the charged fermions only appear as part of the fermion triplet so they are unmixed, so that $M_{\chi^\pm} \equiv M_\Sigma$ (for the reader familiarized with supersymmetric models, we note that the dark fermions of our revamped singlet-triplet scotogenic model correspond to the bino and neutral wino fermions).

C. Neutrino sector

One of the most interesting features of the singlet-triplet scotogenic model is its natural generation of neutrino masses at one-loop level, mediated by the scotogenic particles thanks to the $\mathbb{Z}_2$ symmetry. The latter implies that neutrino mass generation cannot take place at tree level, and comes from the one-loop diagrams given in Fig. 2. The resulting neutrino masses are given by [24,30–33,37,38]

$$\mathcal{M}^\nu_{\alpha\beta} = \sum_{n=1,2} \frac{Y^\nu_{\alpha n} Y^\nu_{\beta n}}{32\pi^2} \mathcal{I}_n(m^2_{\chi_n}, m^2_{\eta_R}, m^2_{\eta_I}), \tag{21}$$

where $\alpha, \beta = 1, 2, 3$ are generation indices for the SM leptons, n labels the mass-eigenstate neutral scotogenic fermions, and the function $\mathcal{I}_n(m^2_{\chi_n}, m^2_{\eta_R}, m^2_{\eta_I})$ is defined as

$$\mathcal{I}_n(m^2_{\chi_n}, m^2_{\eta_R}, m^2_{\eta_I}) = m_{\chi_n}\left(\frac{m^2_{\eta_R}}{m^2_{\eta_R} - m^2_{\chi_n}} \ln\left(\frac{m^2_{\eta_R}}{m^2_{\chi_n}}\right) - \frac{m^2_{\eta_I}}{m^2_{\eta_I} - m^2_{\chi_n}} \ln\left(\frac{m^2_{\eta_I}}{m^2_{\chi_n}}\right)\right). \tag{22}$$

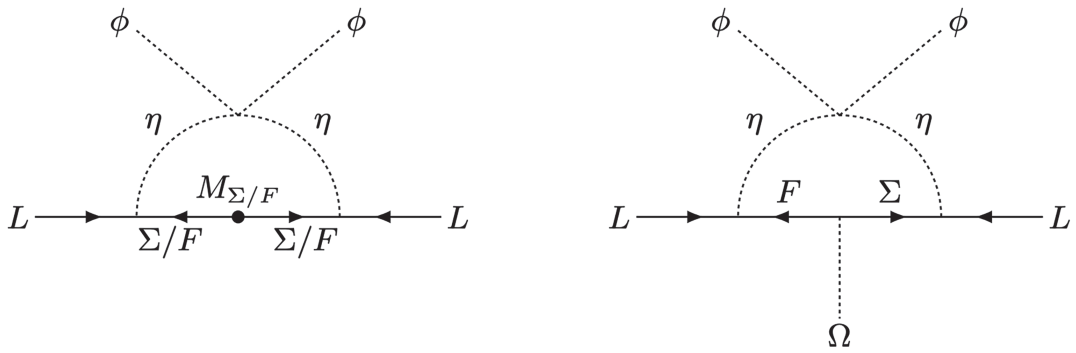


FIG. 2. Radiative neutrino mass generation in the revamped or singlet-triplet scotogenic model.

The Yukawa coupling matrix $Y^{\nu}_{\alpha\beta}$ describing the neutrino/dark sector interaction is given as

$$Y^{\nu}_{\alpha\beta} = \begin{pmatrix} Y^1_\Sigma & Y^1_F \\ Y^2_\Sigma & Y^2_F \\ Y^3_\Sigma & Y^3_F \end{pmatrix} V(\theta). \tag{23}$$

Here $V(\theta)$ is the 2×2 orthogonal matrix that diagonalizes the dark fermion mass matrix of Eq. (19). Notice that Eq. (21) can be cast as a type-I seesaw mass relation,

$$\mathcal{M}^{\nu}_{\alpha\beta} = Y^{\nu}_{\alpha\beta} v_\phi \frac{\mathcal{F}}{v_\phi^2} (Y^{\nu}_{\alpha\beta})^T v_\phi \sim m_D \frac{1}{m_R} m_D^T, \tag{24}$$

where the "Dirac-like" mass term is given by $m_D = Y^{\nu}_{\alpha\beta} v_\phi$ and $m_R^{-1} = \mathcal{F}/v_\phi^2$, with $\mathcal{F}$ defined as

$$\mathcal{F} = \begin{pmatrix} \frac{\mathcal{I}_1}{32\pi^2} & 0 \\ 0 & \frac{\mathcal{I}_1}{32\pi^2} \end{pmatrix}. \tag{25}$$

In order to compare with neutrino oscillation data, it is convenient to express the neutrino Yukawa *à la* Casas-Ibarra [39],

$$Y^{\nu}_{\alpha\beta} = U_\nu \sqrt{m_\nu}\, \rho \sqrt{\mathcal{F}}^{-1}, \tag{26}$$

where U_ν is the lepton mixing matrix, m_ν is the diagonalized neutrino mass matrix, and ρ is a real 3×2 matrix that will depend on the mass hierarchy of the neutrinos,

$$\rho = \begin{pmatrix} 0 & 0 \\ \cos\omega & \sin\omega \\ -\sin\omega & \cos\omega \end{pmatrix} (\mathrm{NO}),$$
$$\rho = \begin{pmatrix} \cos\omega & \sin\omega \\ -\sin\omega & \cos\omega \\ 0 & 0 \end{pmatrix} (\mathrm{IO}), \tag{27}$$

where ω can be a complex angle, and NO and IO refer to normal and inverse ordering, respectively.

An interesting feature about the mass generation in the singlet-triplet scotogenic model is the fact that the lightest neutrino is massless. This follows from the fact that there are two dark fermions (F and Σ) coupling to the three left-handed neutrinos, i.e., one of the neutrinos has no partner and remains massless, similar to the tree-level "missing partner seesaw" called (3,2) in the generalized type-I seesaw discussed in Ref. [26]. As we already discussed, the parameter λ_5 plays a key role in the generation of neutrino masses. If one takes the limit $\lambda_5 \to 0$, the masses of the neutral states η_I and η_R becomes equal according to Eqs. (17) and (18). In this case $\mathcal{M}^{\nu}_{\alpha,\beta} \to 0$; see Eq. (22). As this restores lepton number conservation, the choice of a small value of λ_5 can be considered natural in the sense of 't Hooft [36].

III. CONSTRAINTS

To ensure the consistency of the theory, and to be in agreement with experimental observations, the singlet-triplet scotogenic model is subject to a number of constraints.

(i) Theoretical constraints: Concerning the scalar potential, the constraints discussed in Sec. II should be fulfilled. For instance, by imposing the conditions given in Eq. (4), we also ensure the potential to be bounded from below. Concerning interaction strengths, we enforce perturbativity by assuming the quartic couplings to be $\lesssim 4\pi$. Similarly, for the Yukawa couplings, we assume $Y^{\nu}, Y_N, Y_\Sigma, Y_\Omega \lesssim \sqrt{4\pi}$. The running of the parameters at high energies may lead to the breaking of the $\mathbb{Z}_2$ symmetry. Nonetheless, this can be avoided by choosing $\mu^{\eta}_{\Omega} \lesssim \mathcal{O}(1\ \mathrm{TeV})$. This last constraint could be overrestrictive, since UV completions of the model can lead to new degrees of freedom that prevent the potential breaking of the $\mathbb{Z}_2$ symmetry.

(ii) Neutrino oscillations: A primary goal of the scotogenic model is to generate neutrino masses, so we require that our model fulfills the restriction from neutrino oscillation experiments. In the following,

we assume the preferred normal neutrino mass ordering. In order to fit the experimental values, we make use of Eq. (26) to obtain the neutrino Yukawa matrices by using the best-fit central values taken from Ref. [25], with the squared-mass differences $\Delta m^2_{21} = 7.5 \times 10^{-5}$ and $\Delta m^2_{31} = 2.55 \times 10^{-3}$ eV^2, the mixing angles satisfying $\sin^2\theta_{12} = 0.318$, $\sin^2\theta_{13} = 0.022$, and $\sin^2\theta_{23} = 0.574$, and the CP phase given by $\delta = 1.08\pi$.

(iii) Lepton flavor violation: Within the simplest SM extensions with Dirac neutrino masses, lepton flavor violation processes are highly suppressed due to the Glashow-Iliopoulos-Maiani mechanism. However, in the singlet-triplet scotogenic model, these rare processes may be substantially enhanced [31,40] depending on the masses of the new particles and their Yukawa couplings, $Y_{\Sigma,F}$. As these are directly involved in neutrino mass generation, the negative results of lepton flavor violating processes can also impose indirect restrictions on the λ_5 parameter [40]. In this work, we adopt the three most stringent bounds on lepton flavor violation processes, $\mathrm{BR}(\mu \to e\gamma) \lesssim 1.5 \times 10^{-13}$ (BR stands for branching ratio) [41], $\mathrm{BR}(\mu \to eee) \lesssim 1.0 \times 10^{-12}$ [42], and $\mathrm{CR}(\mu, \mathrm{Au} \to e, \mathrm{Au}) \lesssim 7.0 \times 10^{-13}$ (CR stands for conversion rate) [43].

(iv) Electroweak precision observables: Our model introduces new $SU(2)_L$ multiplets, with an impact on the electroweak observables. The presence of a Higgs triplet in addition to the Higgs doublet affects the ρ parameter according to

$$\rho = \frac{\sum_i c_i \langle \phi_i^0 \rangle^2 [T_i(T_i+1) - Y_i^2]}{2\sum_i \langle \phi_i^0 \rangle^2 Y_i^2} = 1 + 4\frac{v_\Omega^2}{v_\phi^2}, \quad (28)$$

where c_i is a constant that depends on the representation of ϕ_i, $\langle \phi_i^0 \rangle$ is the VEV of the neutral component of the scalar field, T_i is the weak isospin, and Y_i is the hypercharge. In our revamped scotogenic model $i = \phi, \Omega$, the two Higgs boson species present in Table I. The precise measurement of $\rho = 1.00031 \pm 0.00019$ [44], imposes a stringent constraint on the VEV of the Higgs triplet, namely, $v_\Omega \lesssim 4$ GeV, given the real nature of the Higgs triplet. Moreover, the presence of other particles can modify the values of the commonly known oblique parameters (S, T, U). In particular, the charged and neutral components of the η doublet can directly affect the T parameter. From the current values of the T parameter, it follows that the mass splitting should be smaller than $m_{\eta^\pm} - m_{\eta^0} \lesssim 140$ GeV [45]. In our work, as we assume that all λ_i parameters have values allowed by perturbativity. From Eqs. (16)–(18), it is easy to see that the above restriction on the mass splitting is expected to hold.

(v) Dark matter: The $\mathbb{Z}_2$ symmetry allows the LSP to be a good candidate for dark matter, whose relic density depends on parameters such as λ_5, the Yukawa couplings of the new dark fermions, $Y_{\Sigma,F}$ and Y_Ω. Together, they determine the efficiency of the annihilation of the LSP into SM particles in the early Universe, while physical parameters such as the masses of the dark particles and the Higgs bosons can enhance the annihilation cross section. For our analysis, we determine the predicted dark matter relic abundance Ωh^2 using the publicly available tool micrOMEGAs 5.3.41 [46]. We search for points where Ωh^2 is at most 0.120 ± 0.001, which corresponds to the value reported by the Planck experiment [47]. For DM densities below this quantity, a viable dark matter theory would require another DM component such as the axion. We find that in our scheme the relic density restrictions play an important role in quantifying DM detectability by nuclear recoil.

(vi) Colliders: Searches for new particles have been performed at existing colliders, with no evidence yet. This lack of signal allows the relevant experiments to impose bounds on various particles according to their charge and nature. For example, LEP has imposed bounds on different charged particles, either scalars [48–51] or fermions [52–55]. In accordance with this, we take the limit to charged particles to be $m_{H^\pm,\eta^\pm,\chi^\pm} \geq 100$ GeV. Concerning the LHC searches, we will make a complete analysis in the following section, where we will test different scenarios against the current LHC searches from ATLAS and CMS using the software tool CheckMATE [56]. Our revamped scotogenic model also predicts the presence of a triplet scalar that mixes with the Higgs doublet. This can lead to deviations of the Higgs boson properties with respect to those measured at the LHC. It also predicts the appearance of a second neutral Higgs-like state, together with a charged one that can also be produced in the LHC. In order to test our extended Higgs sector at the LHC, we make use of the public code HiggsTools [57], that compares the SM-like Higgs boson deviations to those measured at the LHC using HiggsSignals v.3 [58–61] and HiggsBounds v.6 [62–68]. In particular, deviations of the SM-like Higgs boson decays are heavily constrained by measurements of the decay into photons, $h \to \gamma\gamma$ and into invisible particles, $h \to \chi_1^0\chi_1^0$, where χ_1^0 denotes the LSP.

IV. COLLIDER PHENOMENOLOGY

In this section, we will study the collider phenomenology of the revamped or singlet-triplet scotogenic model. The model includes new triplet fields in comparison with the minimal scotogenic model, as seen in Table I. Apart from

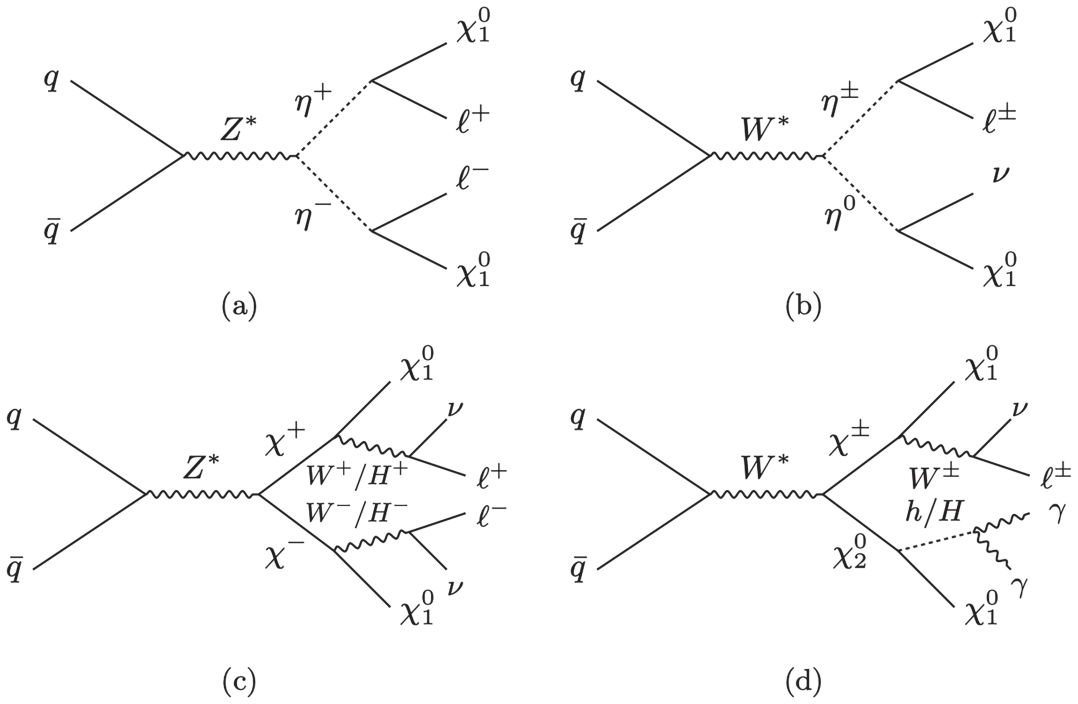


FIG. 3. Relevant diagrams of the production and subsequent decay of the scotogenic particles at the LHC. (a),(b) Production of the scalar doublet η, leading to dilepton plus $E_{\mathrm{T}}^{\mathrm{miss}}$ and monolepton signatures. (c),(d) Production of the fermionic states $\chi^{\pm}$,χ_2^0, leading to dilepton plus $E_{\mathrm{T}}^{\mathrm{miss}}$ and one lepton $E_{\mathrm{T}}^{\mathrm{miss}}$ and a Higgs boson decaying into two photons.

affecting physical observables, the enlarged particle content and their couplings substantially enrich the phenomenology expected at colliders such as the LHC. Details will depend strongly on the assumed mass spectrum. Thanks to the $\mathbb{Z}_2$ symmetry, all interactions must contain an even number of dark particles, so these will always be produced in pairs. In order to investigate the different collider signals, we choose the LSP to be the lighter neutral component of the fermionic triplet and singlet χ_1^0. This choice is motivated by the fact that the fermionic LSP is a suitable candidate for dark matter, fulfilling all the constraints and reproducing the dark matter relic density in a rich variety of spectrum configurations [31]. In particular, we will explore three characteristic benchmark points defined by their spectrum and hence by the hierarchy of the parameters of the Lagrangian[2]:

(A) Heavy dark scalar doublet $(M_F < M_\Sigma \ll m_\eta)$: This first case is characterized by having the scalar doublet decoupled, while both fermionic triplet and singlet mass terms lie at low scales. This configuration corresponds to a dominant χ^+ channel.

(B) Heavy dark triplet fermion $(M_F < m_\eta \ll M_\Sigma)$: The second benchmark has the fermionic triplet decoupled, while the scalar doublet and the singlet fermion are at low energies, resulting in an η^+ channel.

(C) Light dark sector $(M_F < m_\eta \simeq M_\Sigma)$: The third benchmark is characterized by having the fermionic triplet and the scalar doublet at low scales, while the fermionic singlet is fixed at low mass. This means that we allow for both χ^+ and η^+ to be dominant production channels at colliders.

The relevant diagrams for this process are given in Fig. 3. Production at the LHC is driven mainly by gauge boson exchange, as both the scalar and fermionic scotogenic states have gauge couplings. The scalar doublet η has two main production modes indicated as in Figs. 3(a) and 3(b). The fermion production mechanisms include two charged states $\chi^+\chi^-$ and also the production of a charged state and the heavier neutral state $\chi^\pm\chi_2^0$, denoted by Figs. 3(c) and 3(d).[3] The production of two neutral states can also be present; however, the cross section is typically too small in comparison with the other ones. For the case of the η production, we can see in Fig. 3(a) that, once the charged states are produced, they will decay into two leptons plus missing transverse energy $E_{\mathrm{T}}^{\mathrm{miss}}$ associated with the lightest scotogenic particle. When the charged and the neutral states

[2]We discard the case where $m_\eta \ll M_F, M_\Sigma$, as we focus on fermionic dark matter scenarios. For a thorough dark matter and LHC phenomenological study of this scenario, we refer the reader to Ref. [30]. Note also that benchmark cases below bear close analogy with supersymmetric (SUSY) bino dark matter.

[3]In principle, the production of a $\chi^\pm$ and the lighter χ_1^0 is also possible, nonetheless, given the fact that the latter is mainly singlet, the production cross section gets heavily suppressed.

are produced as in Fig. 3(b), only the charged state will decay into a charged lepton, while the neutral state will decay into a neutrino and the lightest neutral fermion, giving large amount of $E_{\mathrm{T}}^{\mathrm{miss}}$, leading to a monolepton signature. For the case of fermionic states being produced, the decay is more complex. In Fig. 3(c), we can see that, once the charged states are produced, they will decay through a W boson. These decays lead to a dilepton plus $E_{\mathrm{T}}^{\mathrm{miss}}$ signature. The production of a charged and neutral fermionic state is more interesting, as can be seen in Fig. 3(d). Here the charged dark fermion decays in the same fashion as before, while the neutral one decays into a Higgs boson. We now exploit one of the cleanest Higgs boson decay modes into two photons in order to explore this production mechanism.

For each scenario, we have performed a scan over the relevant parameters and then simulated 1×10^5 collider events to test each of the chosen benchmark points. Our approach consists of performing grid scans for each scenario varying different parameters, namely, M_F, M_Σ, and m_η, using the spectrum generator SPheno 4.0.5 [69,70]. For each grid point, we have simulated the production of $\chi^\pm\chi^\mp$, $\chi^\pm\chi^0$, $\chi^0\chi^0$, $\eta^\pm\eta^\mp$, $\eta^\pm\eta^0$, and $\eta^0\eta^0$ pairs and their subsequent decays using MadGraph_aMC@NLO_v3.5.1 [71,72] and PYTHIA 8.306 [73]. Finally, we input the hadronized events to CheckMATE 2.0.37 [56], which makes use of the jet reconstruction tool FastJet 3.2.1 [74] and the fast detector simulator DELPHES 3.5.0 [75] to test the analyzed points against current ATLAS and CMS searches, at a 95% confidence level (CL).

CheckMATE uses different searches from ATLAS and CMS[4]; we restrict our analysis to the 13 TeV searches. From each analysis, there are multiple signal regions designed to be sensitive to the different mass hierarchies and final state topologies. CheckMATE chooses the best signal region of each search that corresponds to the best expected exclusion potential, and the best search is chosen to be the one with the strongest expected exclusion power. For this reason, the total exclusion limit can lead to weaker limits than the ones from a single signal region. However, choosing the limits in this fashion, one can avoid downward fluctuations in the data given the large number of signal regions.

Our limits are obtained by selecting the best search and then comparing our simulated number of signal events with the observed one at 95% confidence level. We use the r prescription,

$$r = \frac{S - 1.96\Delta S}{S_{\mathrm{exp}}^{95}}, \tag{29}$$

where S is the number of simulated signal events, ΔS is the uncertainty due to Monte Carlo (MC) events, which we consider to be the statistical uncertainty, and S_{exp}^{95} is the 95% confidence level limit on the number of signal events given by the experiments. Under this prescription, a data point is regarded as excluded when $r > 1$, meaning that the signal events are in tension with the 95% confidence level of events found in the experimental data.[5] Notice that, as the combination of limits is, in general, not possible, given the lack of public data on the correlation among signal regions, the limits/sensitivities we obtain should be regarded as conservative.

The relevant analysis for our processes are shown in Table III (see below), where we list the considered final states and the color code that we assigned for the figures in the rest of the paper. The main LHC production schemes involve the scotogenic pairs, so the relevant searches are determined by the decays of these pairs. One of the most important searches at LHC is the one studying final states with one lepton, one Higgs boson decaying into a pair of photons, and a large amount of missing transverse energy $E_{\mathrm{T}}^{\mathrm{miss}}$ [79], which was originally intended to study the production and decay of charged and neutral electroweakinos in SUSY. The analysis focuses on the decay of the charged state into a W boson plus missing energy and the decay of the neutral state into missing energy and a Higgs boson that eventually decays into a pair of photons. A strict cut on the invariant mass window of the photons, $105 < m_{\gamma\gamma} < 160$ GeV is imposed, in order to isolate events that come from Higgs boson decays. This cut will be important in our study since this search will be ineffective below the Higgs boson production threshold. Other important searches for our analysis involve multilepton plus $E_{\mathrm{T}}^{\mathrm{miss}}$ [80–82]. These were originally used in the context of SUSY, focusing on the presence of two or three leptons and missing transverse energy coming from the decay of electroweakinos. This search will be relevant to our analysis since our studied scotogenic pairs can decay in a similar fashion. Searches for two leptons with soft transverse momentum [83] are also relevant when the mass differences in the dark sector are small, leading to a small transfer of momentum to the final particles. Specific searches for two τ's plus large $E_{\mathrm{T}}^{\mathrm{miss}}$ [84] can also be important. This search was originally intended to search for pairs of staus, decaying into a pair of τ's. As mentioned above, this final state topology is also present in our model.

As we have stressed, the spectrum under study is similar to the one containing bino and wino and a doublet scalar

[4]A full list of implemented searches in CheckMATE can be found in the GitHub repository: https://github.com/CheckMATE2.

[5]Other prescriptions may be used in order to determine whether a point is excluded or not. As noted in Refs. [76–78], one can choose a region where $0.67 \leq r \leq 1.5$ in which the point is inconclusive due to large uncertainties in the simulation (e.g., choice of parton distribution functions, renormalization and factorization scales, cross section, and generated MC event numbers). Under this prescription, a point is in tension with the experimental data and hence excluded if $r > 1.5$ and allowed if $r < 0.67$.

TABLE II. Benchmark points for the heavy dark scalar doublet scenario with $M_F < M_\Sigma \ll m_\eta$. The two top rows correspond to the scenarios with $v_\Omega = 1.5$ and $\mu_1 = 1.1$ and 137.6 GeV, respectively, while the last row corresponds to the scenario with $v_\Omega = 4$ and $\mu_1 = 54$ GeV. λ_a refers to $\lambda_2, \lambda_3, \lambda_4, \lambda_\Omega^2, \lambda_\Omega^\eta$.

	M_F (GeV)	M_Σ (GeV)	$m_\eta - M_F$ (GeV)	μ_1 (GeV)	μ_2 (GeV)	v_Ω (GeV)	λ_1	λ_a	λ_5	Y_Ω
A1	[10, 500]	[100, 1000]	500	1.1	400	1.5	0.26	0.5	4×10^{-7}	2
A2	[10, 500]	[100, 1000]	500	137.6	400	1.5	0.26	0.5	4×10^{-7}	2
A3	[10, 500]	[100, 1000]	500	54	400	4	0.26	0.5	3.5×10^{-8}	2

lepton within the context of SUSY. Indeed, all searches in Table III were originally aimed at exploring SUSY frameworks. However, in contrast to SUSY, where the various parameters are mostly free, in our case the parameter structure is heavily constrained by neutrino phenomenology, in particular, oscillations, making our model predictable and testable.

A. Heavy dark scalar doublet

In this case, we assume that the scotogenic fermion masses lie at lower values, taking much higher values of m_η according to

$$M_F < M_\Sigma \ll m_\eta. \tag{30}$$

We keep the singlet fermionic state as the lower one in mass (LSP) so as to account for the dark matter candidate. Under this mass hierarchy, the LHC phenomenology will be dictated by Figs. 3(c) and 3(d), with the main production at the LHC involving the pairs $\chi^\pm\chi^\mp$, $\chi^\pm\chi_i^0$, and $\chi_i^0\chi_j^0$, where $i, j = 1, 2$. The first two channels are far larger than the last one, so they will be the predominant ones in the searches. The charged states will decay through a W boson giving $\chi^\pm \to W^*\chi_1^0 \to \ell^\pm\nu\chi_1^0$, while the neutral state will decay through the Higgs states, giving as a result the LSP, χ_1^0, and the decay of the Higgs boson. We analyze three benchmark points for this scenario,[6] listed in Table II, which obey the relevant constraints for a viable dark matter candidate [31]. The difference between the benchmark points lies on the values of v_Ω and μ_1. We have taken two reference values of $v_\Omega = 1.5$ and 4 GeV in agreement with the values of the W mass [44], within 1σ of its experimental measurement [31]. Two benchmarks adopt the same $v_\Omega = 1.5$ GeV, but different values of μ_1, i.e., $\mu_1 = 1.1$ and $\mu_1 = 137.6$ GeV. Both result in a SM-like Higgs boson at 125 GeV, but different H and $H^\pm$ masses.

The constraints we obtain are given in Fig. 4. The left panel corresponds to $\mu_1 = 1.1$ GeV (benchmark A1) while the case $\mu_1 = 137.6$ GeV is shown in the right panel (benchmark A2). Note that our results are given in the $M_\Sigma - M_F$ plane, which is reminiscent of the electroweak gaugino mass parameter space often adopted in the SUSY case. The vertical gray band with up-right hatching in both panels corresponds to a physical mass $m_\chi^\pm \lesssim 100$ GeV, which is ruled out by the charged fermion constraints from LEP [52–55]. On the other hand, the triangular gray region with down-right hatching is excluded as it leads to a charged LSP, not viable as a dark matter candidate. We also show the constraints coming from dark matter relic density, with the gray dotted area indicating regions in the parameter space that exceed the observed central value of $\Omega h^2 = 0.12$. The relevant contributions for the annihilation process in this case are listed in the Appendix. The black solid line shows the total exclusion rate from our analysis, with colored areas corresponding to the parameter regions constrained by different LHC searches. The color code in each case is given in the legend of the panels, and the associated final state is indicated in Table III. For clarity, we display in both panels the tilted line $m_{\chi_2^0} = m_{\chi_1^0} + m_h$, which we will refer to as the Higgs boson threshold line in what follows. Below this line, the decay of χ_2^0 produces an on-shell Higgs boson.

We now focus on scenario A1 in the left panel ($v_\Omega = 1.5$ and $\mu_1 = 1.1$ GeV). Given the relatively small μ_1, this scenario predicts all the Higgs states at low masses, with $m_h \sim m_H \sim m_{H^\pm} \sim 125$ GeV. The presence of multiple low-mass Higgs bosons can be potentially in tension with current LHC data, so we have checked this scenario explicitly using the software HiggsTools [57–68] and found that current LHC constraints are not strong enough to exclude it. Indeed, since the second Higgs field is mostly triplet, its couplings to quarks are highly suppressed. Hence, its direct production at the LHC is negligible, though they can appear as decay products of the produced scotogenic particles.

Coming back to the figure, we see that, in the region below the threshold for Higgs production ($m_{\chi_2^0} < m_{\chi_1^0} + m_h$), the most stringent constraint comes from the 2–3 lepton plus E_T^{miss} search [81], indicated in green, covering up to masses $M_F \leq 185$ GeV. On the other hand, for the region to the right of the Higgs threshold line, where $m_{\chi_2^0} > m_{\chi_1^0} + m_h$, the Higgs boson is produced on shell, making the search for leptons, missing energy, and a Higgs boson decaying into photons important [79], as seen from the blue region in the figure. We can see that for $M_F < 50$ GeV this search

[6]The choices of Y_Ω and v_Ω are made to enhance neutral dark fermion mixing, hence increasing the collider signal.

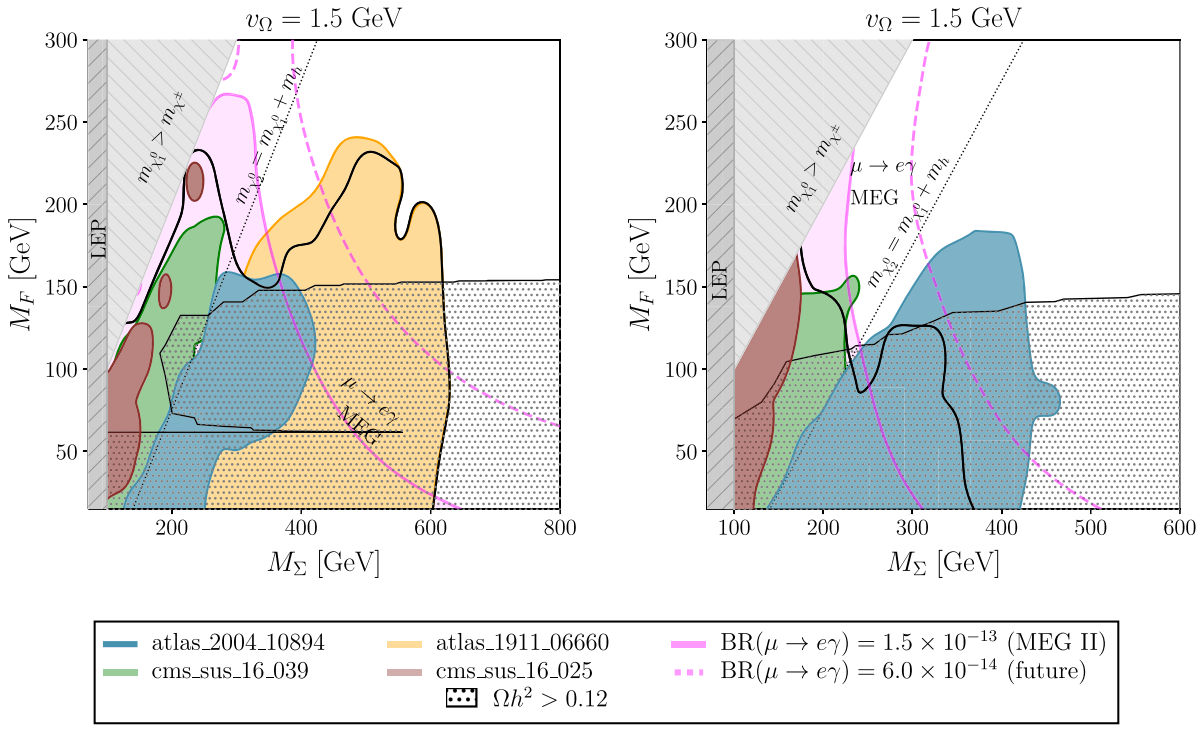


FIG. 4. 95% CL excluded regions in the $M_\Sigma - M_F$ plane for $v_\Omega = 1.5$ GeV: (left) $\mu_1 = 1.1$ and (right) $\mu_1 = 137.6$ GeV. Dashed magenta curves indicate cLFV limits. Notice that the yellow search region is absent from the right panel, due to the parameter choice of the scenario. See text for details.

can constrain up to $M_\Sigma = 250$ GeV, while for masses $M_F > 50$ GeV the limits reach $M_\Sigma = 400$ GeV. This loss of efficiency below $M_F < 50$ GeV reflects the fact that the LSP mass is too small and evades the stringent $E_{\rm T}^{\rm miss}$ cuts used in the analysis. Notice the interesting region covered by the two τ leptons plus $E_{\rm T}^{\rm miss}$ analysis [84] (yellow region in the figure). Here the charged dark fermion can decay to a charged Higgs boson. In fact, once the line $m_{\chi^\pm} = m_{\chi_1^0} + m_{H^\pm}$ is surpassed, one has BR$(\chi^\pm \to H^\pm \chi_1^0) \sim 1$. Indeed, for this scenario the branching fraction into τ's and neutrinos is about BR$(H^\pm \to \tau^\pm \nu_\tau) \sim 0.73$. Hence, in this region, we have $\chi^\pm \chi^\mp$ pair production leading to $\chi^\pm \chi^\mp \to \tau^\pm \tau^\mp \nu_\tau \bar{\nu}_\tau \chi_1^0 \chi_1^0$ as indicated in Fig. 1(c), so we have two τ leptons and $E_{\rm T}^{\rm miss}$ in the final state. This search constrains masses up to $M_\Sigma \sim 600$ and $M_F \sim 240$ GeV.

Moving on to dark matter constraints, notice from the same left panel of Fig. 4 that in this case a large region of the parameter space with M_F below 150 GeV is excluded by relic density. This is explained by the fact that, below this value, the annihilation process in this region is not efficient enough, producing an overabundant dark matter density. However, for low values of M_F and M_Σ, both particles contribute to the relic density in the coannihilation regime [31] and the relic density is in agreement with the observed value. Moreover, the allowed narrow area at $M_F \sim 60$ GeV corresponds to the annihilation through a resonant Higgs ($M_F \sim m_h/2$), where the annihilation process is very effective and the relic density is achieved.

An important feature of scotogenic models, in contrast to WIMP SUSY dark matter, is that in the scotogenic scenario searches for lepton flavor violating processes play a

TABLE III. Summary of the most relevant 13 TeV analyses for our study, sorted by experiment (ATLAS, CMS) with their arXiv or CERN document server numbers. For each analysis, we have written the final state topology of the search. We also give the color scheme used to identify each search.

	Reference	Final state	Color
ATLAS	2004.10894 [79]	$h(\to \gamma\gamma) + (\ell/j) + E_{\rm T}^{\rm miss}$	Dark blue
	1908.08215 [82]	$2\ell + E_{\rm T}^{\rm miss}$	Light blue
	1911.06660 [84]	$2\tau + E_{\rm T}^{\rm miss}$	Yellow
CMS	CMS-PAS-SUS-16-039 [81]	$\geq 2\ell + E_{\rm T}^{\rm miss}$	Green
	CMS-PAS-SUS-16-025 [83]	$2\ell(\text{soft}) + E_{\rm T}^{\rm miss}$	Brown

complementary role to collider studies. We have implemented the relevant cLFV processes making use of the package FlavorKit [85]. Among the different cLFV processes, we found $\mu \to e\gamma$ to be the most constraining, with the current limit from the MEG experiment of $\mathrm{BR}(\mu \to e\gamma) = 1.5 \times 10^{-13}$ [41] shown as a magenta area for benchmark A1. For reference, we also show as a dashed contour the future expected sensitivity of $\mathrm{BR}(\mu \to e\gamma) \approx 6 \times 10^{-14}$ [41]. As we can see, the null cLFV result constrains the range of masses where $M_F \simeq M_\Sigma$. The mass degenerate region is difficult to explore at colliders, since the decay products always carry low momenta. In contrast, however, it produces an enhancement of the cLFV processes. On the other hand, for larger values of M_Σ the LHC searches become more sensitive, while the cLFV searches are less sensitive due to the higher masses involved in the process. Hence, one sees the high degree of complementarity of cLFV experiments with collider searches.

We move now to the right panel of Fig. 4, where we present the results of the benchmark scenario A2 with $v_\Omega = 1.5$ and $\mu_1 = 137.6$ GeV (see Table II). In addition to a SM-like Higgs boson with a mass $m_h = 125$ GeV, this particular value of μ_1 leads to heavy scalars at mass $m_H \simeq 1.4$ TeV for both the neutral H and charged scalar $H^\pm$. As in the previous case, we can divide the parameter space into two areas separated by the Higgs threshold line that allows χ_2^0 to decay into an on shell h. In the region where $m_{\chi_2^0} < m_{\chi_1^0} + m_h$, one can see that searches for two soft leptons and $2/3\ell$ plus $E_{\mathrm{T}}^{\mathrm{miss}}$ are the most sensitive ones. This search is able to constrain up to masses of $M_F \sim 200$ GeV. Once the threshold of the decay into h is reached, this decay will be tagged by the search of one lepton $E_{\mathrm{T}}^{\mathrm{miss}}$ with one Higgs boson decaying to two photons, which is sensitive to masses $150 \lesssim M_\Sigma \lesssim 420$ and $M_F \lesssim 185$ GeV. As in the previous case, one sees here that the cLFV processes can constrain the range of masses where $M_F \simeq M_\Sigma$, showing the complementarity of these searches with those at the LHC. Notice that in this case the total exclusion line does not cover the totality of the yellow region of the individual $2\tau + E_{\mathrm{T}}^{\mathrm{miss}}$ search. This is explained from the analysis using CheckMATE, where the best signal region is considered based on their expected exclusion potential, leading to slight differences between the total exclusion limit and the single signal region.

Concerning the dark matter observables, we see that the relic density constraint excludes the pairs where M_F is small and its difference with M_Σ is large, a region where there is no coannihilation and the LSP cross section is not efficient. Moreover, comparing this case with benchmark A1, we notice that here we do not have a region allowed through Higgs resonance. This is mainly because in this case the mostly triplet Higgs field mass is large. Moreover, the small value of v_Ω and the higher value of μ_1 result in a negligible coupling between the LSP and the doubletlike Higgs field, forbidding the resonant Higgs field channel.

Finally, in Fig. 5 we show the results for the benchmark point A3 in Table II, with $v_\Omega = 4$ GeV. From Eq. (19), one sees that higher v_Ω values increase the mixing between the triplet and singlet fermions, affecting the corresponding phenomenology. In the region where $m_{\chi_2^0} < m_{\chi_1^0} + m_h$, the main searches involve two leptons and $E_{\mathrm{T}}^{\mathrm{miss}}$ constraining masses up to $M_F \sim 120$ GeV (green region), while the soft leptons search constrains masses up to $M_F \sim 150$ GeV (brown region). Once the Higgs boson is kinematically accessible, the most sensitive search is the one looking for a Higgs particle decaying into photons, one lepton, and $E_{\mathrm{T}}^{\mathrm{miss}}$ covering masses up to $M_\Sigma \lesssim 375$ and $M_F \lesssim 140$ GeV.

If we compare this scenario with those with a smaller value of v_Ω in Fig. 4 (benchmarks A1 and A2), we notice that the constraints imposed by LHC searches on the fermion masses are now weaker. This is due to the fact that a larger v_Ω gives a higher mixing between the triplet and singlet fermions. This affects directly the production of the $\chi^\pm$ and χ_2^0 states, reducing the production cross section at the LHC and, consequently, the number of produced signal events. On the same figure, we show again the cLFV constraints as a magenta area. As in the previous cases, the cLFV processes cover the regions where both fermion masses are close, not reaching those areas where there is a big difference in masses, where LHC searches are very sensitive. Finally, we show as a dotted area in Fig. 5 the region excluded by the relic abundance measurement, with the relevant contributions to the annihilation process listed in the Appendix. We see that the constrained area covers the values of M_F that are small as in the previous cases. However, for this case the high value of $v_\Omega = 4$ GeV allows h to have a larger triplet component, opening the Higgs resonant channel in the LSP annihilation in the early Universe.

B. Heavy dark triplet fermion

This benchmark is characterized by the decoupling of M_Σ, leaving the fermion singlet and the scalar doublet masses to low energies,

$$M_F < m_\eta \ll M_\Sigma. \tag{31}$$

As in the previous benchmark, we study the regions where the singlet fermion is LSP. From the Lagrangian structure of the singlet-triplet scotogenic model in Eq. (1) and also Table I, we can identify our doublet scotogenic scalar η with left-handed staus of supersymmetry. In this scenario, the processes relevant for the LHC phenomenology are determined by Figs. 3(a) and 3(b). The production of two neutral scalar states is also possible; however, its cross section is much smaller than those containing one or two charged states. Once a charged state is produced, it will decay into a charged lepton and the LSP, $\eta^\pm \to \ell^\pm \chi_1^0$, while the neutral state will decay into a neutrino and the LSP,

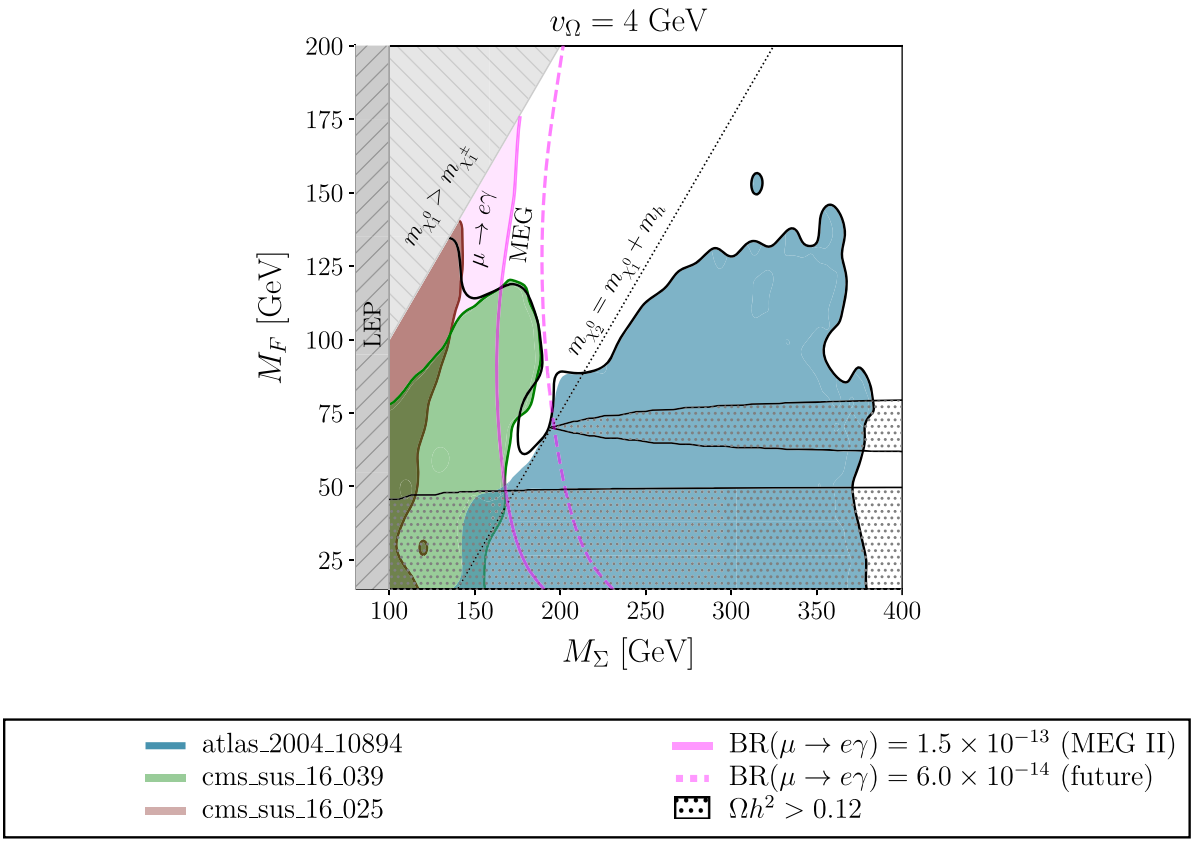


FIG. 5. Excluded regions at a 95% CL in the plane $M_\Sigma - M_F$ for the scenario with $v_\Omega = 4$ and $\mu_1 = 54$ GeV. Dashed magenta curves indicate cLFV limits. See details in text.

$\eta^0 \to \nu\chi_1^0$. The parameters used in this scenario are listed in Table IV.

Figure 6 shows the results of the LHC searches for this benchmark scenario displayed in the m_η-M_F plane. As in the previous plots, the dark gray area with up-right hatching correspond to the LEP limit on charged particles [48–51], while the light gray area with down-right hatching is where χ_1^0 is no longer the LSP. There are two main searches that are important for this scenario. The first one is the search for two leptons and $E_{\rm T}^{\rm miss}$ [82] and the second one is for two τ's plus $E_{\rm T}^{\rm miss}$ [84], which involves the process in Fig. 3(a). Since the main decay of $\eta^\pm$ is into τ leptons, BR$(\eta^\pm \to \tau^\pm\chi_1^0) \simeq 0.64$, the most sensitive search in this scenario is the one looking for two τ's plus $E_{\rm T}^{\rm miss}$ [84] in the final state (yellow area). This search is able to constrain only two small regions between $m_\eta = (140\text{–}165)$ and $m_\eta = (215\text{–}225)$ GeV for low M_F values.

The poor coverage of this search can be explained in terms of the experimental results. Following up on the SUSY analogy, we note that the search for direct stau production was reported in Ref. [84], with the stau decaying into τ leptons and missing energy. The results in Ref. [84] show that the left-handed staus can only be detected in a range of masses between 150 and 300 GeV, assuming that they have a branching fraction of 1 into τ's. Note that the scalar η would have a production rate similar to that of staus at the LHC, but with a lower branching fraction into τ's implying a smaller coverage. Moreover, the difference in the total exclusion rate (black) and the search exclusion rate (full yellow) is due to the difference between the expected and observed signal regions of Ref. [84] as can be seen in Fig. 6.

The total exclusion region is shown as a solid black line. Moreover, as an illustration of the sensitivity of the searches, we also show the exclusion contours for $r = 0.67$ as dashed

TABLE IV. Benchmark point for the heavy dark triplet fermion scenario. Here λ_a denotes $\lambda_2, \lambda_3, \lambda_4, \lambda_\Omega^2, \lambda_\Omega^\eta$.

M_F (GeV)	m_η (GeV)	$M_\Sigma - M\eta$ (GeV)	μ_1 (GeV)	μ_2 (GeV)	v_Ω (GeV)	λ_1	λ_a	λ_5	Y_Ω
[10, 500]	[100, 1000]	500	54	400	4	0.26	0.5	2×10^{-8}	2

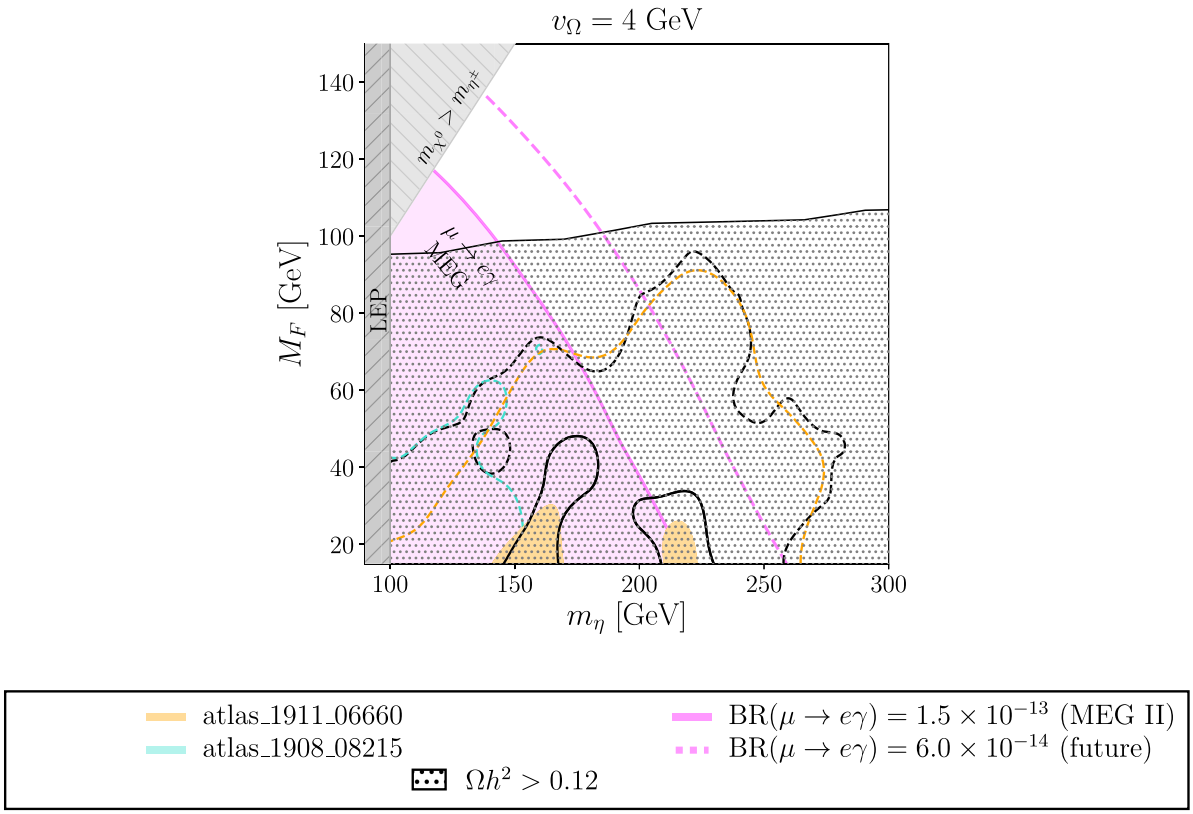


FIG. 6. Excluded regions at a 95% CL in the plane $m_\eta - M_F$ for the case $v_\Omega = 4$ GeV. The dashed magenta curves indicate cLFV limits. See text for details.

lines. Points in this area could be potentially constrained but, due to uncertainties from the Monte Carlo simulation [76–78], one cannot consider them as excluded. However, it helps to illustrate the future reach of the searches. We note that the search for two leptons plus $E_{\mathrm{T}}^{\mathrm{miss}}$ (cyan) covers the low-mass region up to $m_\eta \sim 150$ and $M_F \sim 60$ GeV, while the search for two τ leptons plus $E_{\mathrm{T}}^{\mathrm{miss}}$ (yellow) constrains masses up to $m_\eta \sim 265$ and $M_F \sim 95$ GeV, in good agreement with the coverage given in Ref. [84].

As in previous cases, we show as a magenta area the constraints from the limit on the charged lepton flavor violating BR$(\mu \to e\gamma)$. This process leads to a more stringent constraint on this scenario in comparison with the LHC, reaching masses up to $m_\eta \sim 215$ GeV for $M_F \sim 15$ and $M_F \sim 110$ GeV for $m_\eta \sim 115$ GeV. In this scenario, the cLFV searches are more sensitive than collider searches at the LHC, due to the large sensitivity of the LFV processes to the masses of the scotogenic particles. Finally, we depict the dark matter constraints as a gray dotted area, again with the contributions to annihilation process given in the Appendix. As we can see, the relic density is only achieved for values of $M_F \gtrsim 100$ GeV. We conclude that, for this specific case, the relic density constraints can set bounds that are stronger than the future LHC and LFV prospects.

C. Light dark sector

For this benchmark, we set all three mass parameters M_F, M_Σ, and m_η at low values. In order to have a viable fermionic dark matter candidate, we set the mass of singlet M_F to be lower than the other two mass parameters. This way, the parameters obey

$$M_F < m_\eta \simeq M_\Sigma. \tag{32}$$

In this benchmark, the main production diagrams are those appearing in Fig. 3. Hence, we expect that the main decay channels are those present in Secs. IV A and IV B.

TABLE V. Benchmark choices for the light dark sector scenario with $M_F < m_\eta \simeq M_\Sigma$. Here λ_a denotes $\lambda_2, \lambda_3, \lambda_4, \lambda_\Omega^2, \lambda_\Omega^\eta$.

M_F (GeV)	M_Σ (GeV)	m_η (GeV)	μ_1 (GeV)	μ_2 (GeV)	v_Ω (GeV)	λ_1	λ_a	λ_5	Y_Ω
10	[100, 1000]	[100, 1000]	54	400	4	0.26	0.5	2×10^{-8}	2
90	[100, 1000]	[100, 1000]	54	400	4	0.26	0.5	2×10^{-8}	2

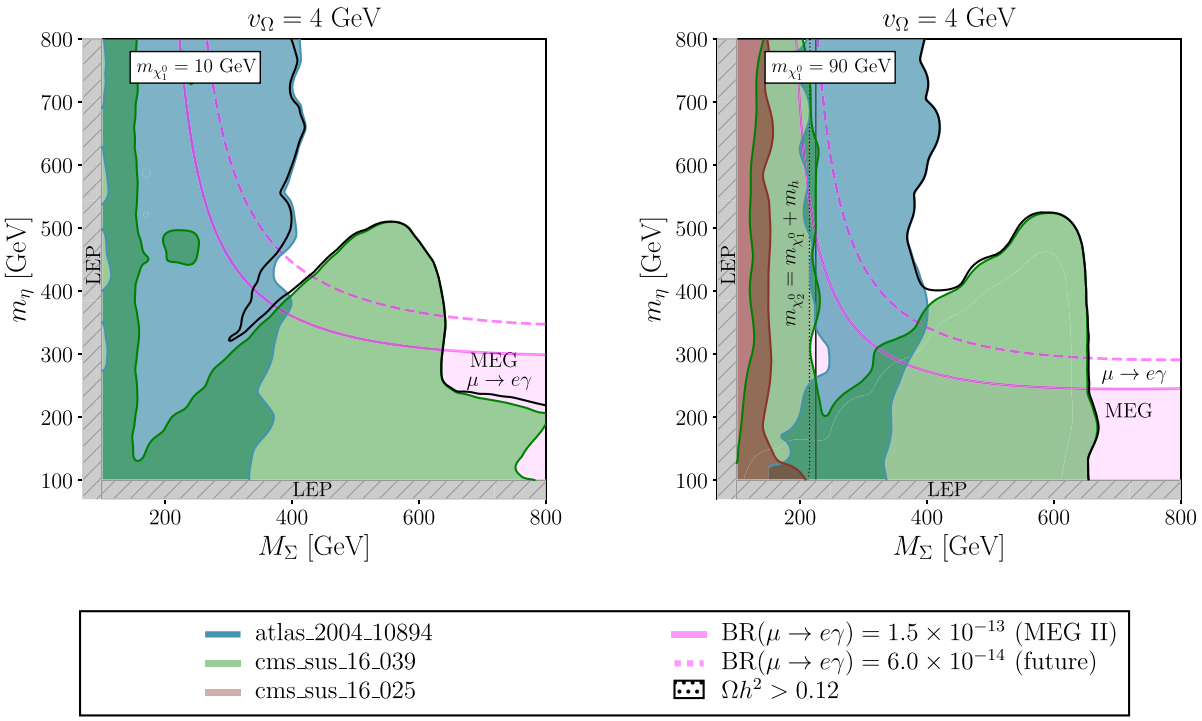


FIG. 7. Excluded regions at a 95% C.L. in the plane $M_\Sigma - m_\eta$. Left: the scenario with $M_F = 10$ GeV. Right: the scenario with $M_F = 90$ GeV.

The parameter space explored in this scenario is shown in Table V.

In Fig. 7, we show the resulting constraints on the plane M_Σ and m_η. In order to study different configurations for this scenario, we choose two values of $M_F = 10$ and 90 GeV. This mass configuration allows the lowest fermionic state to be mostly singlet (LSP). On the left panel of Fig. 7, we show the results for the case where $M_F = 10$ GeV ($m_{\chi_1^0} \simeq 10$ GeV). The search for a Higgs boson and a lepton [79] (blue) covers an area up to $M_\Sigma \simeq 375$ GeV. This search is only sensitive to the triplet fermion, so it is independent of the value of m_η. The other searches that play a role in this scenario are multilepton plus $E_{\mathrm{T}}^{\mathrm{miss}}$ signals [80,81] (green). For low values of M_Σ, they cover an area that is independent of m_η, reaching $M_\Sigma \leq 150$ GeV. For higher masses, one has a triangular area where the main production channel is $\chi^\pm \chi_2^0$. Since $M_\Sigma > m_\eta + M_F$, the relevant decays are $\chi^\pm \to \eta^\pm \nu$ and $\chi_2^0 \to \eta^\pm \ell^\mp$ followed by the subsequent decay of the scalar doublet, $\eta^\pm \to \ell^\pm \chi_1^0$ (see Fig. 8). In this case, the main signal would be 2–3 leptons plus $E_{\mathrm{T}}^{\mathrm{miss}}$, including also τ leptons in the final state, and reaching masses up to $M_\Sigma \sim 600$ GeV. However, when M_Σ reaches the threshold value $M_\Sigma \simeq m_\eta + m_{\chi_1^0}$, the decay is kinematically disfavored, making the search insensitive to that region. A similar behavior is seen when the mass of the singlet is fixed to $M_F = 90$ GeV; see the right panel of Fig. 7. Here the search for a Higgs boson and a lepton [79] (blue) also covers an area that is independent of m_η. In this case, we can see that the search is not sensitive to masses lower than $M_\Sigma \sim 215$ GeV. This is because, for

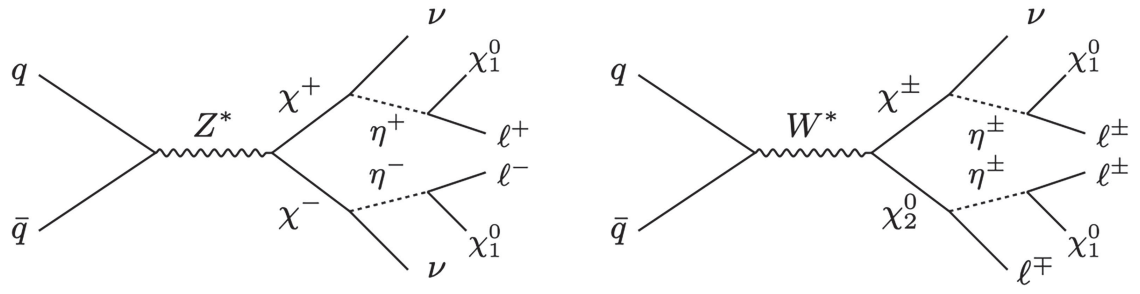


FIG. 8. Relevant diagrams of the production and subsequent decay of the scotogenic particles at the LHC when $M_\Sigma > m_\eta + M_F$. The resulting signal for this configuration is 2–3 leptons plus $E_{\mathrm{T}}^{\mathrm{miss}}$.

$m_{\chi_1^0} \simeq 90$ GeV, the decay $\chi_2^0 \to h\chi_1^0$ produces a low momentum h that cannot be tagged by the analysis. In contrast, for the previous case, the smaller LSP mass allows h to have a greater momentum, leading to a better sensitivity.

The fact that the LSP mass is larger than in the previous case has also consequences for the multilepton searches [80,81] (green). As the LSP mass is greater, this leads to higher missing transverse momenta and hence a better sensitivity of the search, with the upper bound now extended up to $M_\Sigma \sim 220$ GeV. The effect of a greater LSP mass explains also the presence of a lower bound in this case. This search [81] requires leptons to have a minimum transverse momentum of $p_T^\ell > 25$—30 GeV, so when $M_\Sigma - M_F < 30$ GeV, the leptons are not energetic enough to be detected, and therefore, in that area the search is blind. However, searches for soft leptons [83] (brown) are able to cover the lower M_Σ area. In conclusion, in this scenario we can constrain $M_\Sigma < 320$ GeV independent of the value of m_η and also the area under $M_\Sigma < 620$ and $m_\eta < 500$ GeV.

Complementary constraints follow from cLFV processes, e.g., the magenta area for $\mathrm{BR}(\mu \to e\gamma)$. As we can see, the nonobservation of this process rules out larger M_Σ values for $m_\eta < 300$ GeV in the case of $m_{\chi_1^0} = 10$ and 250 GeV for $m_{\chi_1^0} = 90$ GeV. However, for low M_Σ, even though the bounds coming from $\mathrm{BR}(\mu \to e\gamma)$ are strong, LHC constraints are much more sensitive. Notice that in order to fully cover this scenario one needs the complementarity of LHC as well as cLFV searches. It is interesting to remark that, as we have fixed M_F and therefore the value of the LSP mass $m_{\chi_1^0}$, it is difficult to find points in which the relic density is satisfied, except in the case where M_Σ or m_η are close to M_F. However, one can choose a benchmark point, in which the value of M_F, as well as the parameters $Y_{\Sigma,F,\Omega}$ and λ_5 lead to the correct relic density. As we can see from both panels in Fig. 7, the resulting regions constrained from LHC remain very similar for both cases, and one can expect this for other points.

As a last remark, we can explore the projected sensitivity of the High-Luminosity LHC to this model. The HL-LHC is expected to accumulate an integrated luminosity of $\mathcal{L} = 3000$ fb^{-1}. With this amount of data, HL-LHC will explore regions that are inaccessible with the present LHC configuration. We choose the light dark sector scenario as an illustration, since it has all three mass parameters at low values. In Fig. 9, we show the future prospects for the HL-LHC in this scenario as a dashed black line. For comparison, we give the current limits from the 13 TeV LHC data, shown as a red area. The future reach for this scenario will allow us to cover masses up to $M_\Sigma \sim 1150$ and $m_\eta \sim 680$ GeV. This result is almost 2 times the value of M_Σ that can be covered at present. Therefore, if the dark scotogenic sector lies in the TeV range, the HL-LHC will be likely to discover it.

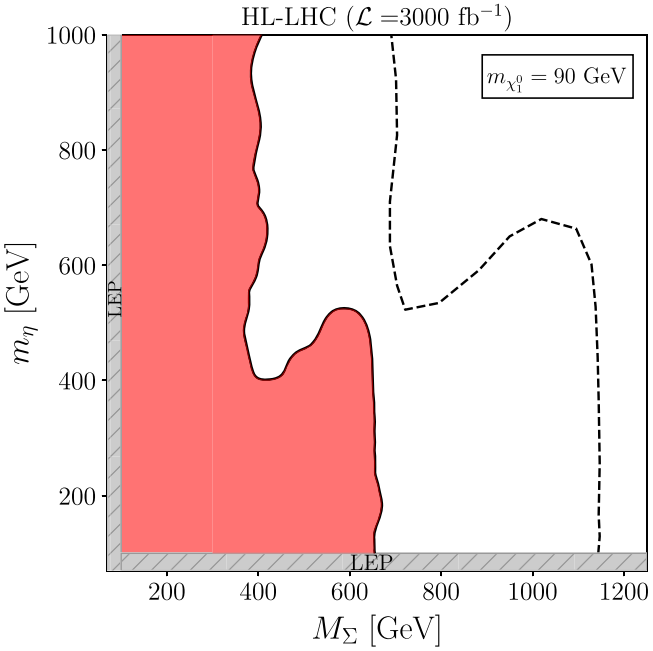


FIG. 9. Excluded regions at a 95% C.L. in the plane $M_\Sigma - m_\eta$ for 13 TeV LHC data (full line and gray area) and prospects for HL-LHC with a luminosity of $\mathcal{L} = 3000$ fb^{-1} for the case with $M_F = 90$ GeV.

V. CONCLUSIONS

We have explored the LHC sensitivity to the revamped (singlet-triplet) scotogenic model [24], where neutrino masses emerge naturally by the radiative exchange of a dark sector in the presence of a conserved $\mathbb{Z}_2$ symmetry. As a follow-up of Refs. [30,37,38], we have now investigated in detail the phenomenological implications of having a fermionic dark matter candidate in this model. In full analogy to the conventional SUSY dark matter scenario, we have now performed a dedicated study of the collider implications of fermionic scotogenic dark matter and contrasted it with complementary charged lepton flavor violation probes. The fermionic nature of the lightest scotogenic particle allows for several spectrum configurations that give rise to a plethora of signals at the LHC.

We have focused on three revamped scotogenic scenarios distinguished by their mass spectrum assumptions. First, we have considered the case of a heavy dark scalar doublet, in which only the singlet and triplet dark fermions are phenomenologically relevant. We found that the LHC sensitivity in this case depends strongly on the assumed values of the parameters v_Ω and μ_1. Our results for this case are summarized in Figs. 4 and 5, depending on the assumed value of v_Ω. The most stringent constraints hold for smaller values of v_Ω and result from searches for leptons and a Higgs boson decaying into two photons.

We also explored the scenario of a heavy dark triplet fermion. In this case, the light degrees of freedom are the

scalar doublet and the singlet fermion. Here the main signal is the production of two scalar doublets decaying into τ leptons and missing transverse energy. From our results, given in Fig. 6, one sees that the sensitivity is poor and only a small region of parameter space is covered. Finally, we studied the scenario where all dark sector states are accessible to the LHC. This case clearly presents a richer phenomenology, with strong constraints, especially on the triplet scalar mass M_Σ, as seen in Fig. 7. We also show in Fig. 9 how the improvements of the HL-LHC can be crucial to unveil the scotogenic nature of dark matter in the future.

Although our analysis is fully analogous to that used in SUSY dark matter scenarios, here dark matter parameters are constrained so as to account for neutrino oscillation experiments. Moreover, they can also be probed through charged lepton flavor violation searches. Indeed, in all of the cases we have analyzed, we found that LHC studies turn out to be complementary to low-energy flavor constraints. Our results indicate that collider sensitivities are fully complementary with those from cLFV experiments, especially the searches for $\mu \to e\gamma$.

ACKNOWLEDGMENTS

We thank Valentina De Romeri for useful discussions about the implementation of the model in SARAH. This work is funded by Spanish Grant No. PID2023-147306NB-I00 and by Severo Ochoa Excellence Grant No. CEX2023-001292-S (MCIU/AEI/10.13039/501100011033) and by Prometeo CIPROM/2021/054 (Generalitat Valenciana). V. M. L. acknowledges the financial support by Ministerio de Universidades and "European Union-NextGenerationEU/PRTR" under the grant María Zambrano UP2021-044 (ZA2021-081). G. S. G. acknowledges financial support by the Grant No. CIAPOS/2022/254 (Generalitat Valenciana).

DATA AVAILABILITY

The data that support the findings of this article are openly available [79,81,83,84].

APPENDIX: DARK MATTER

In this appendix, we show the Feynman diagrams involved in dark matter annihilation in the early Universe, hence relevant for determining its current relic density abundance. There are three different scenarios: single LSP annihilation, coannihilation with the fermionic scotogenic sector, and the coannihilation with the scalar sector.

(i) Single annihilation of the LSP: In this case, the lightest scotogenic particle annihilates into SM particles to provide the relic abundance. We show the main annihilation channels in Fig. 10. The top row shows three diagrams that are mediated by the scotogenic particles in the t and u channels, while the bottom row shows s-channel diagrams mediated by Higgs bosons. These are relevant when the condition $M_F \ll M_\Sigma, m_\eta$ is satisfied, as in our scenarios studied in Secs. IV A and IV B.

(ii) Fermionic coannihilation: If the fermionic sector is close in mass with the LSP then it could also contribute to the annihilation into SM particles [31]. Since the fermionic sector contains both neutral and charged particles, more diagrams contribute to the process when compared to the previous case. The first two rows in Fig. 11 show the t- and u-channel contributions, while the last two rows in the same figure show the s-channel ones. The latter not only involve the neutral Higgs sector but also the charged Higgs and the $W^\pm$ boson. This scenario is achieved when $M_F \leq M_\Sigma$ and it is relevant for our analysis in Secs. IV A and IV C.

(iii) Scalar coannihilation: If the scalar sector is close in mass with the LSP then it will coannihilate with the LSP into SM particles [31]. In the first row of Fig. 12, we show the involved t- and u-channel

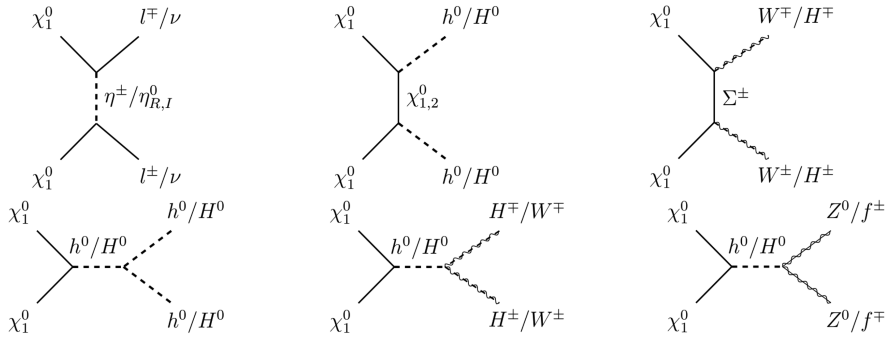


FIG. 10. Diagrams contributing to the annihilation of χ_1^0 in the early Universe. Top row: t- and u-channel annihilation mediated by scotogenic particles. Bottom row: s-channel annihilation mediated by the Higgs sector.

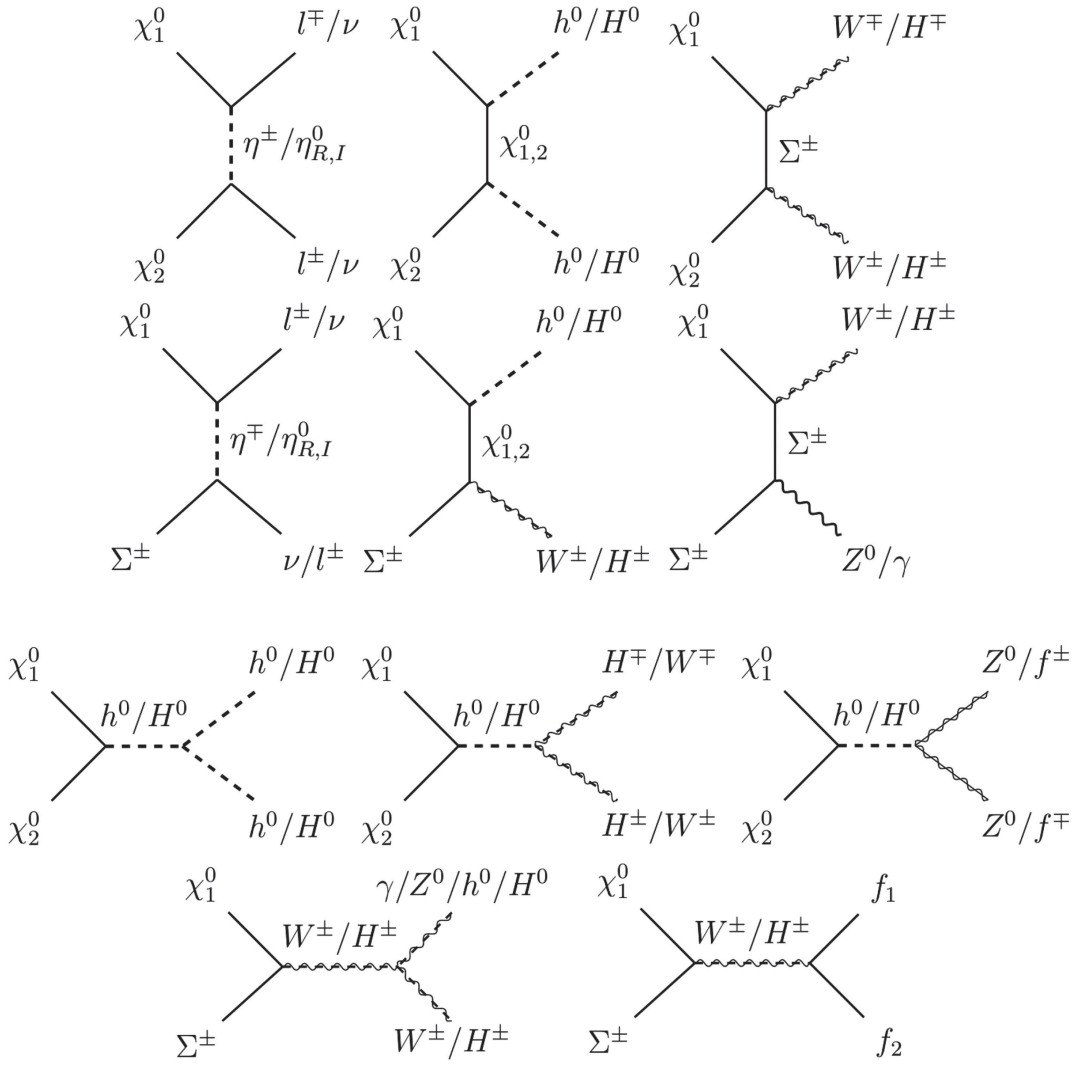


FIG. 11. Diagrams contributing to the fermion-fermion coannihilation. First two rows depict the t and u channels mediated by scotogenic particles, while the last two rows correspond to the s channel mediated by the Higgs sector and W boson.

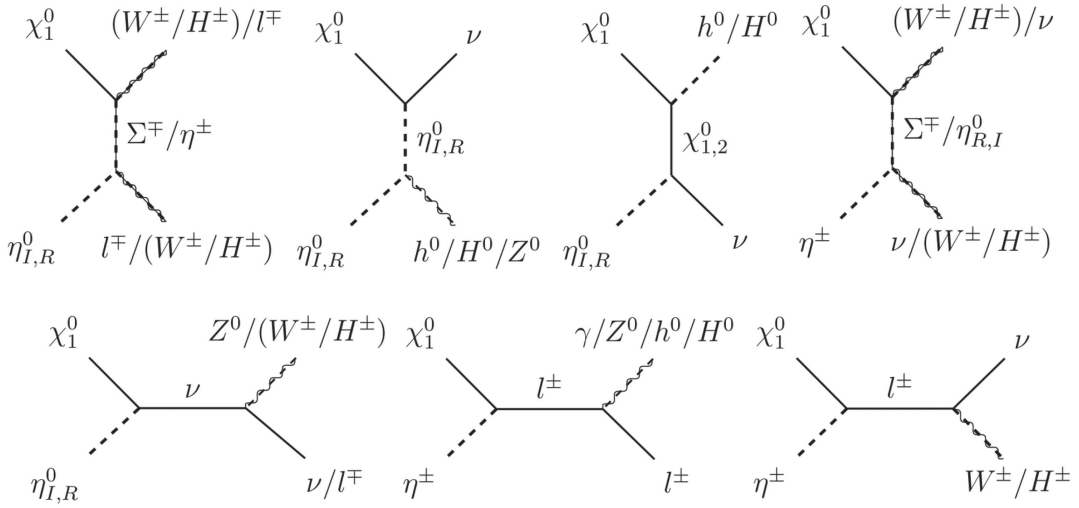


FIG. 12. Diagrams contributing to the scalar-fermion coannihilation. First row shows the t and u channels mediated by scotogenic particles, while the last row corresponds to the s channel mediated by the leptonic sector of the SM.

diagrams that are mediated by scotogenic particles. In addition, the bottom row depicts the s-channel diagrams that, in this specific case, involve the leptonic sector of the SM. This scenario is achieved when $M_F \leq M_\Sigma$ and it is relevant for the analysis in Secs. IV B and IV C.

[1] T. Kajita, Nobel lecture: Discovery of atmospheric neutrino oscillations, Rev. Mod. Phys. **88**, 030501 (2016).
[2] A. B. McDonald, Nobel lecture: The Sudbury Neutrino Observatory: Observation of flavor change for solar neutrinos, Rev. Mod. Phys. **88**, 030502 (2016).
[3] G. Bertone and D. Hooper, History of dark matter, Rev. Mod. Phys. **90**, 045002 (2018).
[4] Z.-j. Tao, Radiative seesaw mechanism at weak scale, Phys. Rev. D **54**, 5693 (1996).
[5] E. Ma, Verifiable radiative seesaw mechanism of neutrino mass and dark matter, Phys. Rev. D **73**, 077301 (2006).
[6] J. Kubo, E. Ma, and D. Suematsu, Cold dark matter, radiative neutrino mass, $\mu \to e\gamma$, and neutrinoless double beta decay, Phys. Lett. B **642**, 18 (2006).
[7] E. Ma and D. Suematsu, Fermion triplet dark matter and radiative neutrino mass, Mod. Phys. Lett. A **24**, 583 (2009).
[8] W. Chao, Dark matter, LFV and neutrino magnetic moment in the radiative seesaw model with fermion triplet, Int. J. Mod. Phys. A **30**, 1550007 (2015).
[9] Y. Farzan and E. Ma, Dirac neutrino mass generation from dark matter, Phys. Rev. D **86**, 033007 (2012).
[10] T. Toma and A. Vicente, Lepton flavor violation in the scotogenic model, J. High Energy Phys. 01 (2014) 160.
[11] S. Fraser, E. Ma, and O. Popov, Scotogenic inverse seesaw model of neutrino mass, Phys. Lett. B **737**, 280 (2014).
[12] A. Merle and M. Platscher, Running of radiative neutrino masses: The scotogenic model—revisited, J. High Energy Phys. 11 (2015) 148.
[13] M. Lindner, M. Platscher, C. E. Yaguna, and A. Merle, Fermionic WIMPs and vacuum stability in the scotogenic model, Phys. Rev. D **94**, 115027 (2016).
[14] E. Ma and O. Popov, Pathways to naturally small Dirac neutrino masses, Phys. Lett. B **764**, 142 (2017).
[15] A. Ahriche, K. L. McDonald, and S. Nasri, The scale-invariant scotogenic model, J. High Energy Phys. 06 (2016) 182.
[16] W. Wang, R. Wang, Z.-L. Han, and J.-Z. Han, The $B - L$ scotogenic models for Dirac neutrino masses, Eur. Phys. J. C **77**, 889 (2017).
[17] D. Borah, P. S. B. Dev, and A. Kumar, TeV scale leptogenesis, inflaton dark matter and neutrino mass in a scotogenic model, Phys. Rev. D **99**, 055012 (2019).
[18] D. Borah, D. Nanda, N. Narendra, and N. Sahu, Right-handed neutrino dark matter with radiative neutrino mass in gauged B − L model, Nucl. Phys. **B950**, 114841 (2020).
[19] K. S. Babu, P. S. B. Dev, S. Jana, and A. Thapa, Non-standard interactions in radiative neutrino mass models, J. High Energy Phys. 03 (2020) 006.
[20] P. Escribano, M. Reig, and A. Vicente, Generalizing the scotogenic model, J. High Energy Phys. 07 (2020) 097.
[21] C. Alvarado, C. Bonilla, J. Leite, and J. W. F. Valle, Phenomenology of fermion dark matter as neutrino mass mediator with gauged B-L, Phys. Lett. B **817**, 136292 (2021).
[22] R. Kumar, N. Nath, and R. Srivastava, Cutting the scotogenic loop: Adding flavor to dark matter, J. High Energy Phys. 12 (2024) 036.
[23] Y. Garnica, A. Morales, and C. A. Vaquera-Araujo, Scotogenic dark matter from gauged $B - L$, arXiv:2411.13756.
[24] M. Hirsch, R. A. Lineros, S. Morisi, J. Palacio, N. Rojas, and J. W. F. Valle, WIMP dark matter as radiative neutrino mass messenger, J. High Energy Phys. 10 (2013) 149.
[25] P. F. de Salas, D. V. Forero, S. Gariazzo, P. Martínez-Miravé, O. Mena, C. A. Ternes, M. Tórtola, and J. W. F. Valle, 2020 global reassessment of the neutrino oscillation picture, J. High Energy Phys. 02 (2021) 071.
[26] J. Schechter and J. W. F. Valle, Neutrino masses in $SU(2) \times U(1)$ theories, Phys. Rev. D **22**, 2227 (1980).
[27] N. Rojas, R. Srivastava, and J. W. F. Valle, Simplest scoto-seesaw mechanism, Phys. Lett. B **789**, 132 (2019).
[28] D. M. Barreiros, R. G. Felipe, and F. R. Joaquim, Combining texture zeros with a remnant CP symmetry in the minimal type-I seesaw, J. High Energy Phys. 01 (2019) 223.
[29] S. Mandal, R. Srivastava, and J. W. F. Valle, The simplest scoto-seesaw model: WIMP dark matter phenomenology and Higgs vacuum stability, Phys. Lett. B **819**, 136458 (2021).
[30] I. M. Ávila, V. De Romeri, L. Duarte, and J. W. F. Valle, Phenomenology of scotogenic scalar dark matter, Eur. Phys. J. C **80**, 908 (2020).
[31] A. Karan, S. Sadhukhan, and J. W. F. Valle, Phenomenological profile of scotogenic fermionic dark matter, J. High Energy Phys. 12 (2023) 185.
[32] A. Merle, M. Platscher, N. Rojas, J. W. F. Valle, and A. Vicente, Consistency of WIMP dark matter as radiative neutrino mass messenger, J. High Energy Phys. 07 (2016) 013.
[33] M. A. Díaz, N. Rojas, S. Urrutia-Quiroga, and J. W. F. Valle, Heavy Higgs boson production at colliders in the singlet-triplet scotogenic dark matter model, J. High Energy Phys. 08 (2017) 017.
[34] J. F. Gunion, R. Vega, and J. Wudka, Higgs triplets in the Standard Model, Phys. Rev. D **42**, 1673 (1990).
[35] J. F. Gunion, H. E. Haber, G. L. Kane, and S. Dawson, *The Higgs Hunter's Guide* (CRC Press, Boca Raton, 2000), Vol. 80.
[36] G. 't Hooft, Naturalness, chiral symmetry, and spontaneous chiral symmetry breaking, NATO Sci. Ser. B **59**, 135 (1980).
[37] S. Choubey, S. Khan, M. Mitra, and S. Mondal, Singlet-triplet fermionic dark matter and LHC phenomenology, Eur. Phys. J. C **78**, 302 (2018).

[38] D. Restrepo and A. Rivera, Phenomenological consistency of the singlet-triplet scotogenic model, J. High Energy Phys. 04 (2020) 134.
[39] J. A. Casas and A. Ibarra, Oscillating neutrinos and $\mu \to e, \gamma$, Nucl. Phys. **B618**, 171 (2001).
[40] P. Rocha-Moran and A. Vicente, Lepton flavor violation in the singlet-triplet scotogenic model, J. High Energy Phys. 07 (2016) 078.
[41] K. Afanaciev *et al.* (MEG II Collaboration), New limit on the $\mu^+ \to e^+\gamma$ decay with the MEG II experiment, arXiv: 2504.15711.
[42] U. Bellgardt *et al.* (SINDRUM Collaboration), Search for the decay $\mu^+ \to e^+e^+e^-$, Nucl. Phys. **B299**, 1 (1988).
[43] W. H. Bertl *et al.* (SINDRUM II Collaboration), A search for muon to electron conversion in muonic gold, Eur. Phys. J. C **47**, 337 (2006).
[44] S. N. *et al.*, The review of particle physics, Phys. Rev. D **110**, 030001 (2024).
[45] A. Abada and T. Toma, Electric dipole moments in the minimal scotogenic model, J. High Energy Phys. 04 (2018) 030; 04 (2021) 060(E).
[46] G. Bélanger, F. Boudjema, A. Goudelis, A. Pukhov, and B. Zaldivar, micrOMEGAs5.0: Freeze-in, Comput. Phys. Commun. **231**, 173 (2018).
[47] N. Aghanim *et al.* (Planck Collaboration), Planck 2018 results. VI. Cosmological parameters, Astron. Astrophys. **641**, A6 (2020); **652**, C4(E) (2021).
[48] A. Heister *et al.* (ALEPH Collaboration), Search for scalar leptons in e^+e^- collisions at center-of-mass energies up to 209-GeV, Phys. Lett. B **526**, 206 (2002).
[49] DELPHI Collaboration, Searches for supersymmetric particles in e^+e^- collisions up to 208-GeV and interpretation of the results within the MSSM, Eur. Phys. J. C **31**, 421 (2003).
[50] P. Achard *et al.* (L3 Collaboration), Search for scalar leptons and scalar quarks at LEP, Phys. Lett. B **580**, 37 (2004).
[51] OPAL Collaboration, Search for anomalous production of dilepton events with missing transverse momentum in e^+e^- collisions at $\sqrt{s} = 183$–209 GeV, Eur. Phys. J. C **32**, 453 (2004).
[52] A. Heister *et al.* (ALEPH Collaboration), Search for charginos nearly mass degenerate with the lightest neutralino in e^+e^- collisions at center-of-mass energies up to 209-GeV, Phys. Lett. B **533**, 223 (2002).
[53] J. Abdallah *et al.*, Searches for supersymmetric particles in e^+e^- collisions up to 208 GeV, and interpretation of the results within the MSSM, Eur. Phys. J. C **31**, 421 (2003).
[54] M. Acciarri *et al.* (L3 Collaboration), Search for charginos with a small mass difference with the lightest supersymmetric particle at $\sqrt{S} = 189$-GeV, Phys. Lett. B **482**, 31 (2000).
[55] K. Ackerstaff *et al.* (OPAL Collaboration), Search for chargino and neutralino production at $\sqrt{s} = 170$-GeV and 172-GeV at LEP, Eur. Phys. J. C **2**, 213 (1998).
[56] D. Dercks, N. Desai, J. S. Kim, K. Rolbiecki, J. Tattersall, and T. Weber, CheckMATE 2: From the model to the limit, Comput. Phys. Commun. **221**, 383 (2017).
[57] H. Bahl, T. Biekötter, S. Heinemeyer, C. Li, S. Paasch, G. Weiglein, and J. Wittbrodt, HiggsTools: BSM scalar phenomenology with new versions of HiggsBounds and HiggsSignals, Comput. Phys. Commun. **291**, 108803 (2023).
[58] P. Bechtle, S. Heinemeyer, O. Stål, T. Stefaniak, and G. Weiglein, HiggsSignals: Confronting arbitrary Higgs sectors with measurements at the Tevatron and the LHC, Eur. Phys. J. C **74**, 2711 (2014).
[59] O. Stål and T. Stefaniak, Constraining extended Higgs sectors with HiggsSignals, Proc. Sci. EPS-HEP2013 (**2013**) 314 [arXiv:1310.4039].
[60] P. Bechtle, S. Heinemeyer, O. Stål, T. Stefaniak, and G. Weiglein, Probing the standard model with Higgs signal rates from the Tevatron, the LHC and a future ILC, J. High Energy Phys. 11 (2014) 039.
[61] P. Bechtle, S. Heinemeyer, T. Klingl, T. Stefaniak, G. Weiglein, and J. Wittbrodt, HiggsSignals-2: Probing new physics with precision Higgs measurements in the LHC 13 TeV era, Eur. Phys. J. C **81**, 145 (2021).
[62] P. Bechtle, O. Brein, S. Heinemeyer, G. Weiglein, and K. E. Williams, HiggsBounds: Confronting arbitrary Higgs sectors with exclusion bounds from LEP and the tevatron, Comput. Phys. Commun. **181**, 138 (2010).
[63] P. Bechtle, O. Brein, S. Heinemeyer, G. Weiglein, and K. E. Williams, HiggsBounds 2.0.0: Confronting neutral and charged Higgs sector predictions with exclusion bounds from LEP and the tevatron, Comput. Phys. Commun. **182**, 2605 (2011).
[64] P. Bechtle, O. Brein, S. Heinemeyer, O. Stal, T. Stefaniak, G. Weiglein, and K. Williams, Recent developments in HiggsBounds and a preview of HiggsSignals, Proc. Sci. CHARGED2012 (**2012**) 024 [arXiv:1301.2345].
[65] P. Bechtle, O. Brein, S. Heinemeyer, O. Stål, T. Stefaniak, G. Weiglein, and K. E. Williams, HiggsBounds-4: Improved tests of extended Higgs sectors against exclusion bounds from LEP, the Tevatron and the LHC, Eur. Phys. J. C **74**, 2693 (2014).
[66] P. Bechtle, S. Heinemeyer, O. Stal, T. Stefaniak, and G. Weiglein, Applying exclusion likelihoods from LHC searches to extended Higgs sectors, Eur. Phys. J. C **75**, 421 (2015).
[67] P. Bechtle, D. Dercks, S. Heinemeyer, T. Klingl, T. Stefaniak, G. Weiglein, and J. Wittbrodt, HiggsBounds-5: Testing Higgs sectors in the LHC 13 TeV era, Eur. Phys. J. C **80**, 1211 (2020).
[68] H. Bahl, V. M. Lozano, T. Stefaniak, and J. Wittbrodt, Testing exotic scalars with HiggsBounds, Eur. Phys. J. C **82**, 584 (2022).
[69] W. Porod, SPheno, A program for calculating supersymmetric spectra, SUSY particle decays and SUSY particle production at e^+e^- colliders, Comput. Phys. Commun. **153**, 275 (2003).
[70] W. Porod and F. Staub, SPheno 3.1: Extensions including flavour, *CP*-phases and models beyond the MSSM, Comput. Phys. Commun. **183**, 2458 (2012).
[71] J. Alwall, R. Frederix, S. Frixione, V. Hirschi, F. Maltoni, O. Mattelaer, H. S. Shao, T. Stelzer, P. Torrielli, and M. Zaro, The automated computation of tree-level and next-to-leading order differential cross sections, and their matching to parton shower simulations, J. High Energy Phys. 07 (2014) 079.
[72] R. Frederix, S. Frixione, V. Hirschi, D. Pagani, H. S. Shao, and M. Zaro, The automation of next-to-leading order electroweak calculations, J. High Energy Phys. 07 (2018) 185; 11 (2021) 085(E).

[73] C. Bierlich *et al.*, A comprehensive guide to the physics and usage of PYTHIA 8.3 SciPost Phys. Codebases **2022**, 8 (2022).
[74] M. Cacciari, G. P. Salam, and G. Soyez, FastJet user manual, Eur. Phys. J. C **72**, 1896 (2012).
[75] J. de Favereau, C. Delaere, P. Demin, A. Giammanco, V. Lemaître, A. Mertens, and M. Selvaggi (DELPHES 3 Collaboration), DELPHES 3, A modular framework for fast simulation of a generic collider experiment, J. High Energy Phys. 02 (2014) 057.
[76] J. S. Kim, M. E. Krauss, and V. Martin-Lozano, Probing the electroweakino sector of general gauge mediation at the LHC, Phys. Lett. B **783**, 150 (2018).
[77] F. Domingo, J. S. Kim, V. M. Lozano, P. Martin-Ramiro, and R. Ruiz de Austri, Confronting the neutralino and chargino sector of the NMSSM with the multilepton searches at the LHC, Phys. Rev. D **101**, 075010 (2020).
[78] J. S. Kim, M. E. Krauss, V. Martín Lozano, and F. Staub, Illuminating stealth scenarios at the LHC, Phys. Rev. D **101**, 035033 (2020).
[79] G. Aad *et al.* (ATLAS Collaboration), Search for direct production of electroweakinos in final states with missing transverse momentum and a Higgs boson decaying into photons in pp collisions at $\sqrt{s} = 13$ TeV with the ATLAS detector, J. High Energy Phys. 10 (2020) 005.
[80] ATLAS Collaboration, Search for direct production of electroweakinos in final states with missing transverse momentum and a Higgs boson decaying into photons in pp collisions at $\sqrt{s} = 13$ TeV with the ATLAS detector, Report No. ATLAS-CONF-2016-096, CERN, 2016, https://cds.cern.ch/record/2212162.
[81] CMS Collaboration, Search for electroweak production of charginos and neutralinos in multilepton final states in pp collision data at $\sqrt{s} = 13$ TeV, Report No. CMS-PAS-SUS-16-039, CERN, 2017, https://cds.cern.ch/record/2256434.
[82] G. Aad *et al.* (ATLAS Collaboration), Search for electroweak production of charginos and sleptons decaying into final states with two leptons and missing transverse momentum in $\sqrt{s} = 13$ TeV pp collisions using the ATLAS detector, Eur. Phys. J. C **80**, 123 (2020).
[83] CMS Collaboration, Search for new physics in the compressed mass spectra scenario using events with two soft opposite-sign leptons and missing transverse momentum at $\sqrt{s} = 13$ TeV, Report No. CMS-PAS-SUS-16-025, CERN, 2016, https://cds.cern.ch/record/2205866.
[84] G. Aad *et al.* (ATLAS Collaboration), Search for direct stau production in events with two hadronic τ-leptons in $\sqrt{s} = 13$ TeV pp collisions with the ATLAS detector, Phys. Rev. D **101**, 032009 (2020).
[85] W. Porod, F. Staub, and A. Vicente, A FlavorKit for BSM models, Eur. Phys. J. C **74**, 2992 (2014).